3D Radiative Heating of Tropical Upper Tropospheric Cloud Systems derived from Synergistic A-Train Observations and Machine Learning

5 Claudia J. Stubenrauch[1], Giacomo Caria[1], Sofia E. Protopapadaki[2], Friederike Hemmer[1]

[1]Laboratoire de Météorologie Dynamique / Institut Pierre-Simon Laplace, (LMD/IPSL), Sorbonne Université, Ecole Polytechnique, CNRS, Paris, France
[2]COOPETIC, Paris, France

Correspondence to: Claudia J. Stubenrauch (stubenrauch@lmd.polytechnique.fr)

10 **Abstract.** Upper Tropospheric (UT) cloud systems constructed from Atmospheric Infrared Sounder (AIRS) cloud data provide a horizontal emissivity structure, allowing to link convective core to anvil properties. By using machine learning techniques we composed a horizontally complete picture of the radiative heating rates deduced from CALIPSO lidar and CloudSat radar measurements, which are only available along narrow nadir tracks. To train the artificial neural networks, we combined the simultaneous AIRS, CALIPSO and CloudSat data with ERA-Interim meteorological reanalysis data in the tropics over a period 15 of four years. Resulting non-linear regression models estimate the radiative heating rates as a function of about 40 cloud, atmospheric and surface properties, with a column-integrated mean absolute error (MAE) of 0.8 K/d (0.5 K/day) for cloudy scenes and 0.4 (0.3 K/day) for clear sky in the longwave (shortwave) spectral domain. Already about 20 basic input variables yield good results, with a 6% (10%) larger MAE. Developing separate models for i) high opaque clouds, ii) cirrus, iii) mid- and low-level clouds and iv) clear sky, independently over ocean and over land, lead to a small improvement, when considering 20 the profile shapes. These models were then applied to the whole AIRS cloud dataset, combined with ERA-Interim, to build 3D radiative heating rate fields. Over the deep tropics, UT clouds have a net radiative heating effect of about 0.3 K/day throughout the troposphere from 250 hPa downward, with a broad maximum of about 0.4 K/d around 330 hPa, enhancing the column-integrated latent heating by about 25%. This value is larger than earlier results of about 20%. Above the height of 200 hPa, the LW cooling above convective cores and thick cirrus anvils is opposed by thin cirrus heating. Whereas in cooler regions 25 low-level clouds also influence the net radiative heating profile, in warmer regions it is nearly completely driven by deep convective cloud systems. These mesoscale convective systems (MCS) are colder and include slightly more thin cirrus around their anvils than those in cooler regions. Hence, the MCSs over these warmer regions produce a vertically more extended heating by the thicker cirrus anvils and a heating of 0.7 K/d above the height of 200 hPa by the surrounding thin cirrus. The roughly estimated horizontal gradients between cirrus anvil and convective core as well as between surrounding thin cirrus and cirrus anvil seem to be slightly smaller in warmer regions, which can be explained by their larger coverage. The 15-year 30 time series of the heating / cooling effects of MCSs are well related to the ENSO variation. While the coverage of all MCSs is

relatively stable (or very slightly decreasing) with surface warming, with -1.3 ± 0.6 %/K, the coverage of cold MCSs relative to all MCSs significantly increases by +18 ± 5 %/K.

1 Introduction

35 Upper tropospheric (UT) clouds play a vital role in the climate system by modulating the Earth's energy budget and the UT heat transport. These clouds cover about 30% of the Earth and even 40% of the tropics (e. g. Stubenrauch et al. 2013, 2017). Yet, their role in the climate change feedback is still highly uncertain (e. g. Boucher et al., 2013, Zelinka et al., 2016). Tropical organized deep convection leads to cloud systems with stratiform cirrus anvils of the size of several 1000's km^2 (e.g. Houze, 2004). Living much longer than the convective towers themselves, these cirrus anvils produce a radiative heating that is

40 expected to be as important for the large-scale circulation as the released latent heat in the initial stage of convection. In tropical convective regions more than 50% of the total heating is contributed by cirrus radiative heating (e.g. Sohn 1999). This heating, induced by the anvils and cirrus, then influences the large-scale tropical atmospheric circulation (e.g. Slingo and Slingo, 1991; Sherwood et al., 1994). It is affected by: i) the areal coverage, ii) the horizontal cloud emissivity structure within the systems, and iii) the vertical structure of the cirrus anvils (layering and microphysics). The influence of the vertical distribution of

45 radiative heating was demonstrated on large-scale tropical circulations by Stephens and Webster (1984) and Bergman and Hendon (2000) and on the local cloud structure by Mather et al. (2007). The net radiative heating associated with tropical anvils and cirrus layers is also known to play a major role in the thermodynamic stability of the upper troposphere (Ackerman et al., 1988) and self-regulation of tropical convection (e.g. Stephens et al., 2004, 2008).

So far, observational studies of tropical mesoscale convective systems (MCSs) have concentrated on the convective towers

50 and the thick cirrus anvils (e.g. Yuan and Houze 2010, Roca et al. 2014). Yet thin cirrus correspond to about 30% of / around the anvil area of the deep convective systems (Protopapadaki et al. 2017). Other studies, focusing on their vertical structure along narrow nadir tracks (Fig. 1), missed the lateral horizontal dimension (e.g. Igel et al., 2014; Stein et al. 2017). The organisation of convection was studied by statistical analysis of ‒cloud regimes‖ defined by similar cloud property distributions within grid cells (e.g. Tselioudis et al. 2013, Tan et al. 2015, Oreopoulos et al., 2016). Suggesting a connection between

55 radiative effects and dynamics, this concept is very valuable, but it misses the horizontal extent of the systems.

A study by Li et al. (2013) finds that the column-integrated radiative heating of tropical UT clouds accounts for about 20% of the latent heating. The radiative heating was estimated by combining International Satellite Cloud Climatology Project (ISCCP) data, classified as four distinct cloud regimes at a spatial resolution of 2.5° latitude and longitude, with heating rate profiles assigned from two tropical Atmospheric Radiation Measurement (ARM) sites, while the latent heating was deduced

60 from measurements of the Tropical Rainfall Measuring Mission (TRMM) Precipitation Radar (PR). However, ISCCP and ARM data both may underestimate the effect of thin cirrus, because its occurrence may be missed by ground observation

(Protat et al., 2014) and by ISCCP (e.g. Stubenrauch et al., 2013), in particular when low-level clouds are also present and during night.

Therefore, to include also the thinner cirrus and the complete 3D structure of these cloud systems, we applied a different
65   strategy: To estimate the radiative heating rates of UT clouds we combined observations which are more sensitive to thin cirrus, together with machine learning techniques and a cloud system approach. The good spectral resolution of IR sounders makes them sensitive to cirrus, down to a visible optical depth of 0.2, during daytime and nighttime. Cloud properties retrieved from measurements of the cross-track scanning Atmospheric Infrared Sounder (AIRS) aboard the polar orbiting Aqua satellite have a large instantaneous horizontal coverage (Stubenrauch et al., 2017). They have been used by Protopapadaki et al. (2017)
70   to reconstruct UT cloud systems. Recently these datasets have been extended, so that they now cover Sep 2002 to Aug 2019. On the other hand, the space-borne active lidar and radar measurements of the CALIPSO and CloudSat missions (Stephens et al., 2002) supply the cloud vertical structure, in particular the radiative heating rates (Henderson et al., 2013). As this information is only available along successive narrow nadir tracks, separated by about 2500 km, we employed machine learning techniques on cloud, atmospheric and surface properties to build a 3D description of these cloud systems. These
75   techniques were already successfully applied to extend IR brightness temperature (Kleynhans et al., 2017) and snow water (Snauffer et al., 2018) from other atmospheric variables.

This article presents the effect of UT clouds on tropical radiative heating rates in the longwave (LW) and shortwave (SW) spectral domain and the relationship between surface temperature, convective depth and anvil radiative heating / cooling. Data and Methods are described in Section 2. Sensitivity studies and evaluation of the developed non-linear regression models via
80   machine learning are presented in Section 3. They give insight into the most appropriate cloud and atmospheric properties as well as on how many scene-dependent non-linear regression models are necessary to reliably predict the radiative heating rates of different cloud types and of clear sky, over ocean and land. After application of these models to the AIRS cloud and ERA-Interim atmospheric and surface data, section 4 investigates the contribution of clouds and in particular of thin cirrus and MCSs on the radiative heating / cooling. Conclusions and outlook are given in Section 5.

85   **2 Data and Methods**

2.1 AIRS Cloud Data and Cloud System Data

Since 2002 AIRS (Chahine et al., 2006) aboard the National Aeronautics and Space Administration (NASA) Earth Observation Satellite Aqua provides very high spectral resolution measurements of Earth emitted radiation in the thermal IR (3.74 ó 15.40 μm) at 1:30AM and 1:30PM local time (LT). Cross-track scanning leads to a large instantaneous coverage of about 70% in
90   the tropics. The spatial resolution of these measurements at nadir is about 13.5 km. Nine AIRS measurements (3 x 3) correspond to one footprint of the Advanced Microwave Sounder Unit (AMSU).

3

The Clouds from IR Sounders (CIRS) data (Stubenrauch et al., 2017) provide cloud pressure (p_{cld}), cloud emissivity (ε_{cld}), as well as cloud temperature (T_{cld}) and cloud height (z_{cld}), together with their uncertainties. The cloud retrieval is based on a weighted χ^2 method (Stubenrauch et al., 1999), which uses eight channels along the 15 μm CO_2 absorption band, with peak

95 contributions coming from 235, 285, 375, 415, 565, 755, 855 hPa and near the surface. Minimizing χ^2 leads to a pair of p_{cld} and ε_{cld} values. The uncertainty on p_{cld} is estimated by identifying the pressure level at which the normalized weighted $\chi_{norm}^2(p)$ = $(\chi^2(p) - \chi_{min}^2)/(\chi_{max}^2 - \chi_{min}^2)$ reaches 0.025, a value empirically determined by Feofilov et al. (2017). The uncertainty on ε_{cld} is then determined as the difference between ε_{cld} and the value of ε_{cld} computed at this pressure level. UT (high-level) clouds are defined as clouds with p_{cld} < 440 hPa. UT cloud types are further distinguished with respect to ε_{cld} as opaque high clouds

100 (Cb, ε_{cld} × 0.98), cirrus (Ci, 0.98 < ε_{cld} Ö 0.5) and thin cirrus (thCi, 0.5 < ε_{cld} Ö 0.1). p_{cld} is transformed to T_{cld} and z_{cld} via the atmospheric temperature and water vapour profiles of the ancillary data (see section 2.2). An ‒a posterioriø multi-spectral cloud detection is based on the spectral coherence of retrieved cloud emissivity in the atmospheric window between 9 and 12 μm. This spectral region also provides information on the thermodynamic phase of the clouds, and for semi-transparent cirrus the slope of cloud emissivities between 9 and 12 μm gives an indication of the effective ice crystal diameter (Guignard et al. 2012).

105 To get information on the surrounding cloud scene structure within a region of 2° latitude x 2° longitude, we distinguished sixteen cloud regimes by applying a k-means clustering on histograms of ε_{cld} and p_{cld} from CIRS-AIRS data, similar to the method developed by Rossow et al. (2005) using ISCCP data. In addition, we provide the clear sky fraction estimated from AIRS within these grid cells.

The reconstruction of UT cloud systems is based on two independent variables, p_{cld} and ε_{cld} (Protopapadaki et al. 2017): The

110 AIRS cloud data were first merged to grid cells of 0.5° latitude x 0.5° longitude, and only grid cells with more than 70% UT clouds were used to reconstruct UT cloud systems. After having filled the data gaps between adjacent orbits, UT cloud systems were built from adjacent elements of similar cloud height, given by p_{cld}; in a second step convective cores, thick cirrus and thin cirrus were identified within the anvils by using ε_{cld}. This cloud system approach was used in section 4 to identify MCSs and to relate the radiative heating / cooling profiles of their convective cores and their anvils to different surface conditions.

115 Therefore MSCs were defined as UT cloud systems with at least one convective core (built from grid cells with average ε_{cld} > 0.98 within subregions of ε_{cld} > 0.9) and a core fraction within the system of at least 0.05.

2.2 Atmospheric and surface data

ERA-Interim (Dee *et al.* 2011) is a global atmospheric reanalysis provided by the European Centre for Medium-Range Weather Forecast (ECMWF). Land surface, oceanographic, atmospheric, and spaceborne measurements from numerous sources are

120 assimilated in the Integrated Forecast System. The data assimilation scheme is sequential: at each time step, it exploits available observations to constrain the model, which in turn provides a short-range forecast for the next assimilation time step. Gridded

data products (at a spatial resolution of 0.75° latitude x 0.75° longitude) include 6-hourly surface temperature, atmospheric temperature and water vapour profiles, as well as dynamical parameters such as horizontal and vertical large-scale winds. These data are given at Coordinated Universal Time (UTC) values of 0:00, 6:00, 12:00 and 18:00. In order to match these

125 data with the AIRS observations, the former were interpolated to the corresponding local time, using a cubic spline function, as in Aires *et al.* (2004). Surface temperature and pressure, atmospheric profiles of temperature and water vapour, interpolated to 23 pressure levels, and tropopause pressure determined from the temperature profile according to Reichler et al. (2003) were added, since the CIRS retrieval relies on these ancillary data for the retrieval (Stubenrauch et al., 2017). We then derived the relative humidity within the 22 atmospheric layers from the temperature and water vapour profiles by a method based on

130 (Stubenrauch and Schumann, 2005). The CIRS cloud retrieval classifies the temperature and water vapour profiles by comparing them to about 2300 representative clear sky atmospheric profiles of the Thermodynamic Initial Guess Retrieval (TIGR) data base (Chédin et al. 1985, 2003), which includes the spectral atmospheric transmissivities used in the radiative transfer part of the retrieval. This atmospheric classification provides additional information for the non-linear regression models developed in section 3.

135 Spectral IR surface emissivities over land have been retrieved in the case of clear sky conditions using measurements of the IR Atmospheric Sounding Interferometers (IASI) by Paul et al. (2012). We use a monthly mean climatology at a spatial resolution of 0.25° x 0.25° for wavelengths with values around 9.00, 10.16and 12.18 μm. The surface emissivity of water is set to 0.99 for 9 μm and to 0.98 for the other wavelengths, according to Wu and Smith (1997).

For the prediction of the SW heating rates during daytime we use, instead of the spectral IR surface emissivities, the visible

140 surface albedo at noon local solar time and the solar zenith angle. The land surface albedos, retrieved under clear sky conditions at wavelengths of visible light measured by the Moderate Resolution Imaging Spectroradiometer (MODIS) sensors on NASA⊘s Aqua and Terra satellites (MODIS Collection 5, MOD43 product, Strahler et al., 1999), are distributed as a monthly climatology at a spatial resolution of 0.1° x 0.1° by the NASA Earth Observations (NEO) website (https://neo.sci.gsfc. nasa.gov/). Over ocean we assume a surface albedo at noon local solar time of 0.06.

145 MODIS also provides aerosol optical depth (AOD) at a wavelength of 550 nm (MODIS Collection 5, MOD04/MYD04 product, Levy et al., 2009). We explore the benefit of adding the AOD of a monthly climatology at a spatial resolution of 0.25° x 0.25°, also provided by the NEO website, to the input variables to be used by the machine learning.

Finally we explore the value of adding the vertical velocity at 500 hPa, at the spatial resolution of 0.375° x 0.375°, from the ERA5 reanalysis (Hersbach et al., 2020).

150 **2.3 CALIPSO-CloudSat vertical structure and collocation with AIRS**

The vertical structure of the clouds can only be determined by active spaceborne instruments. The Cloud-Aerosol Lidar with Orthogonal Polarization (CALIOP) aboard CALIPSO and the Cloud Profiling Radar (CPR) aboard CloudSat, both part of the

A-Train constellation, follow AIRS within a few minutes. CALIOP (Winker et al., 2009) provides backscatter profiles at a wavelength of 532 nm and 1064 nm, with a vertical and horizontal resolution of about 30 m and 90 m, respectively.

155 Measurements are sampled every 333 m along the track. The backscatter ratio helps to distinguish between aerosols and clouds. The 94 GHz nadir-viewing CPR (Stephens et al., 2002) measures profiles of the power backscattered by clouds at a native vertical resolution of 480 m over footprints covering 1.8 km×1.4 km. By using oversampling, data are provided at a vertical resolution of 240 m. While CALIOP is even sensitive to subvisible cirrus, its signal only penetrates clouds to a level where the cloud gets opaque (i. e. the optical depth reaches about 3). On the other hand, CPR is able to probe optically thick cloud

160 layers and therefore provides their correct cloud base. By combining information from both instruments it is possible to describe completely the vertical structure of clouds. However, this information is only given along successive nadir tracks.

The radiative fluxes and heating rates of 2B-FLXHR-LIDAR (version R04; Henderson et al., 2013; L'Ecuyer et al., 2008) were derived by applying the BUGSrad broadband radiative transfer model (Ritter and Geleyn, 1992) to the scenes observed by CALIPSO-CloudSat, using as inputs the vertical location of the cloud layers (2B-GEOPROF-LIDAR), the cloud water /

165 ice content and effective particle sizes retrieved from radar only (2B-CWC-RO) (Austin et al., 2009), distinction between cloud and rain water contents from 2C-PRECIP-COLUMN (Haynes et al, 2009) and collocated atmospheric and surface auxiliary data from ECMWF. For the clouds and aerosols which are undetected by CloudSat, the MODIS-based cloud optical depth (2B-TAU) and CALIPSO version-3 products (Trepte et al., 2010) are used to calculate the corresponding radiative properties. Thin clouds which are only detected by CALIPSO are defined as ice clouds by a temperature smaller than 253.15

170 K, and their ice crystal equivalent mass sphere effective radius is assumed to be 30 μm for the radiative transfer calculations. According to a study of Protat et al. (2014) over the tropical ARM site of Darwin, the shapes of the radiative heating rates are in good agreement with those derived from ground-based remote sensing by radiative transfer calculations (McFarlane et al., 2013) and with those from an experimental 2C-ICE-FLUX product, between altitudes of 1 and 12 km. Above 12 km, ice properties included from 2C-ICE lead to a reduced LW cooling and enhanced LW warming of about 0.3 K/day compared to

175 2B-FLXHR-LIDAR, whereas the underreported cirrus frequency by the ground-based lidar at the ARM site leads to an enhanced LW cooling and reduced LW warming of about 0.4 to 0.8 K/day.

The 2C-ICE-FLUX product assumes different cloud microphysical and radiative properties than the 2B-FLXHR-LIDAR data, in particular the ice microphysical properties are obtained from 2C-ICE (Deng et al., 2013), when 2B-CWC-RO has no data. The same microphysical properties, together with improved cloud phase identification and surface characteristics, are

180 integrated in the very recently released version R05 of FLXHR-LIDAR data (Matus and L'Ecuyer, 2017). The improvements led to a better agreement with TOA fluxes from the Clouds and the Earth's Radiant Energy System (CERES), with global annual mean TOA net cloud radiative effect of -17.1 ± 4.2 Wm^{-2} (Matus and L'Ecuyer, 2017) compared to -18.1 ± 3.7 Wm^{-2} (Henderson et al., 2013) and global annual mean atmospheric cloud radiative effect between both versions differing by about 10% (Hang et al., 2019): 7.8 Wm^{-2} (R05) compared to 8.6 Wm^{-2} (R04).

185 The comparison of 2B-FLXHR-LIDAR (R04) with CERES-CALIPSO-CloudSat-MODIS (CCCM) products, using a finer vertical resolution and different microphysics than FLXHR-LIDAR, revealed a small low bias in SW heating of FLXHR-LIDAR due to a slight underestimation of cloud occurrence of height below 1 km, while the LW heating of CCCM for thin cirrus may be slightly high biased (Ham et al., 2017).

We extended the collocated AIRS-CALIPSO-CloudSat data used by Feofilov et al. (2015) and Stubenrauch et al. (2017) by
190 the NASA 2B FLXHR-LIDAR (R04) heating rates for the period of 2007 to 2010. These are given at a vertical resolution of 240 m, corresponding to about 80 values over a height of 20 km. Since the AIRS cloud height is retrieved as pressure and the input parameters are probably not precise enough to predict such a fine vertical structure, we transformed the FLXHR-LIDAR heating rates to 22 pressure layers between 70 hPa and the surface. For each of the AIRS footprints this collocated dataset also includes the number of detected cloud layers, as well as cloud top and cloud base of each of these cloud layers, detected by
195 lidar or radar, at the spatial resolution of the radar footprints from the 2B-GEOPROF-LIDAR data. In section 3 we use the number of detected cloud layers to evaluate the clear sky identification by AIRS alone.

As version R05 of the FLXHR-LIDAR data was only released when we were finishing our analyses of section 4, we present the results which used 2B-FLXHR-LIDAR (R04) data for the training of the artificial neural networks (ANN), keeping in mind that the cirrus HRs above a height corresponding to 200 hPa are more reliable than those from ground-based measurements by
200 may be still slightly underestimated compared to newer versions with different ice microphysics (Protat et al., 2014; Ham et al., 2017; Hang et al., 2019). Within the overall uncertainties described in this section and in section 3, the results in Section 4 are still valid. In the future we will train the ANN models again with the improved version of the FLXHR-LIDAR data and a new version of the CIRS data (using ERA5 ancillary data, as ERA-Interim data production ceased in August 2019).

2.4 Artificial Neural Network Construction

205 The challenge in creating a complete 3D description of the UT cloud systems and their environment lies in the lateral expansion of the information on the vertical structure, only available at the locations sampled along the lidar-radar nadir tracks, illustrated in Figure 1. In order to achieve this goal, we developed nonlinear regression models based on ANNs on the combined AIRS and ERA-Interim data as described in sections 2.1 and 2.2. ANNs have seen spectacular progress during the last few years, especially in the automation of finding the most appropriate weights used in the ANN layers. We used the TensorFlow
210 framework (https://www.tensorflow.org) to train machine learning models available in the Keras program library (https://keras.io) for Python, with training and testing along the nadir tracks, using four years of collocated data.

Kleynhans et al. (2017) demonstrated that thermal IR radiation at top of atmosphere, as measured by MODIS, can be best simulated from available atmospheric reanalysis data by using a multi-layer perceptron (MLP) supervised learning technique. This technique produced the lowest overall error rates, in particular over cloudy situations, compared to non-linear support
215 vector regression (SVR), convolutional neural network (CNN) and even to atmospheric radiative transfer simulations. After

having explored the performance on the number of hidden layers within the MLP ANN, our final ANN consists of an input layer with the approximately 30 to 45 input variables (see section 3), two hidden layers with 64 neurons and an output layer which corresponds to the radiative heating rates given in 22 pressure layers. Hsieh (2009) states that often a single hidden layer is already adequate to model any nonlinear continuous function. To improve the performance, we used the rectified linear unit

220   (ReLU) activation function, corresponding to $max(0,x)$. For a better efficiency we use the Adaptive Moment Estimation (Adam) optimizer, using adaptive learning rates (Kingma and Ba, 2014).

The training dataset is randomly separated into three portions: 80% are used for training, 10% for validation and 10% for testing. In order to have similar cloud type, day-night and ocean-land statistics in these portions, we stratified the data by cloud type, ocean-land and day-night for LW and by cloud type and ocean-land for SW (only available during daytime). We used

225   the mean absolute error (MAE) between the prediction and the target value from the lidar-radar observations as metrics for the quality of the regression model.

The input variables have first been normalized by subtracting the mean and dividing by the standard deviation over the four-year dataset. However, this metrics is difficult to use in phase 2, when we apply the model to all data, because in this case we would need to re-compute the mean and standard deviation of each variable over the whole data period, as they may change

230   with time. In addition, not all input variable distributions are Gaussian. Therefore, once we had established sensitivity tests to estimate the most appropriate variables, we trained final scene-dependent models by standardizing the input variables, which means subtraction of an acceptable minimum and division by the difference between acceptable maximum and minimum. These acceptable minimum and maximum values have been established for each variable and adapted to the scenes for which the models were trained: ocean or land, all cloud types, clear sky, high clouds or mid- and low-level clouds. Before the

235   application of the model, the input variables have been bounded between minimum and maximum in order to avoid outliers.

3 Evaluation and Sensitivity Studies

In this section we assess the sensitivity of the predicted radiative heating rates (HRs) to two different factors: the selection of input variables and the number of scene types for which the models are developed. The following cloud scenes are considered: i) all clouds over the whole tropical band, ii) all clouds separately over ocean and over land, iii) high-level clouds and

240   independently mid- / low-level clouds, each of both cloud types separately over ocean and over land and iv) Cb, Ci / thin Ci, mid- / low-level clouds independently, where each cloud type is further separated over ocean and over land. Clear sky is treated independently, because the cloud properties are not used in this case. For the application to all data, the cloud and clear sky models are then combined to construct the radiative HRs over the whole tropical band (section 3.3).

3.1 Sensitivity to input variables

245 The input variables describing the cloud, atmosphere and surface properties used for the prediction of the radiative HRs are summarized in Table 1.

The training for the SW HRs is based only on data recorded at 1:30PM LT, while the training for the LW HRs exploits data for both 1:30AM and 1:30PM. Since the CALIPSO data are slightly more sensitive during night-time, we used for the LW training a day-night flag as additional input variable. The choice of input variables slightly differs for the prediction of LW

250 and SW HRs: For the training of LW HRs, we used surface spectral IR emissivities while for the training of SW HRs we used surface albedo and solar zenith angle.

The MLP regression models compute from about 40 input variables radiative HRs for 22 pressure layers from 70 hPa to 1000 hPa. Earth topography implies that the temperature, relative humidity and radiative HR profiles are not always determined over all 22 pressure layers. Given that neural networks need a constant number of input and output values, we had to replace

255 the missing values below the surface. Therefore, we first continued the temperature, relative humidity and radiative HR profiles below p_{surf} with their lowest valid value, and then added to these values the average vertical gradients between the corresponding layer and the layer with the lowest valid value. These gradients were computed using the average profiles of regions containing all 22 pressure layers, separately determined over ocean and over land, and per cloud type and month. Even if these values below the surface are not used in the analyses, they slightly influence the training.

260

Table 1: List of input variables for the prediction of LW and SW heating rates.

Clouds	
CIRS cloud properties and uncertainties	ε_{cld}, p_{cld}, T_{cld}, $d\varepsilon_{cld}$, dp_{cld}, dT_{cld}, χ_{min}^2
cloud spectral emissivity difference	(ε_{cld} (12μm) - (ε_{cld} (9μm))
CIRS cloud regime (CR) at 2° x 2°	CR (1-16), kernel distance
Atmosphere	
AIRS T_B at 0.5° x 0.5°	T_B(11.85μm), $\sigma(T_B)$, T_B(7.18 μm)
ERA-Interim atmospheric properties	TIGR atmosphere (1-1500), total precipitable water, $p_{tropopause}$
ERA-Interim relative humidity profile	RH (determined from T and water vapour) within 10 layers
ERA-Interim temperature profile	T within 10 layers
ERA5 vertical velocity	ω at 500hPa
MODIS aerosol optical depth	AOD (monthly mean climatology)
Surface	
ERA-Interim surface properties	p_{surf}, T_{surf}, nb of atm. layers down to p_{surf}
IASI spectral surface emissivity	ε_{surf}(9, 10, 12μm) (monthly mean climatology)
surface albedo	α_{surf} (monthly mean climatology)
solar zenith angle, day-night flag, land-ocean flag	

For the sensitivity study of the most appropriate variables, we considered cloudy scenes over ocean, and we set up six different
280   experiments to predict the LW (SW) HRs, starting with

1) a set of 18 (19) basic variables, which describe cloud, atmospheric and surface properties: CIRS cloud properties and their
uncertainties, cloud spectral emissivity difference between 9 and 12 μm, AIRS brightness temperatures, total precipitable
water, tropopause height and TIGR atmosphere class, surface pressure and temperature.

Then we gradually added to the basic variables of experiment 1:

285   2) weather state classification and its uncertainty given by the kernel distance: total of 20 (21) input variables,

3) relative humidity in ten layers: total of 30 (31) input variables,

4) atmospheric temperature in ten layers: total of 40 (41) input variables,

5) vertical velocity from ERA5 reanalyses: total of 41 (42) input variables, and

6) monthly mean aerosol optical depth: total of 42 (43) input variables.

290   Table 2 compares the mean absolute error (MAE) for the prediction of LW and SW heating rates of clouds over ocean from
the experiments 1 to 6. In all cases the MAE over the validation data and over the testing data are within 0.01 K/d. Therefore
only the MAE over the validation dataset is shown. We provide further details in Figure S1 of the supplement, presenting the
MAE as a function of number of iterations (epochs). The similarity in MAE between the validation and testing data means that
there is no under-fitting (the variables are not sufficient to predict the target) nor over-fitting (the model is too detailed, with
295   too many variables or the data base is not sufficiently large). A similar figure for the evaluation of the clear sky models is
given in Figure S2 of the supplement. As shown in Table 2, the MAE decreases by about 5% (10%) for the LW (SW) model
when the atmospheric profiles are included, while the addition of vertical velocity and AOD do not seem to improve the results.
This lack of improvement may be explained by noise coming from these sources in combination with the AIRS cloud properties
and ERA-Interim atmospheric and surface properties. The addition of the temperature profile only slightly improves the
300   prediction of the heating rates, most probably because the atmospheric T profiles are more similar within the tropics than the
atmospheric relative humidity profiles.

Table 2: MAE (K/d) for the prediction of LW or SW heating rates of clouds over ocean, from experiments 1 - 6.

ocean	basic	+ WS	+ RH10	RH-T10	+ w500	+ AOD
LW HR	0.84	0.84	0.80	**0.79**	0.79	0.79
SW HR	0.51	0.50	0.46	**0.45**	0.45	0.45

305 As the MAE only provides an average estimation of the quality of the prediction, we also considered the difference between the predicted radiative HRs and those determined from CALIPSO-CloudSat measurements over tropical ocean, separately for five cloud types: high opaque (Cb), cirrus (Ci), thin cirrus, midlevel and low-level clouds. The LW and SW results are compared between the different experiments in Figure S3 of the supplement. Overall, all results show good agreement between predicted and CALIPSO-CloudSat derived HRs. The differences between mean predicted and ÷observedø radiative HRs

310 undulate well around 0 K/day. However, we note that when using the ERA5 vertical velocity at 500 hPa as an additional input variable, the results for Cb and mid- and low-level clouds in the LW are slightly degraded. Similarly, the addition of the monthly mean AOD does not improve the results. This indicates only a medium compatibility between these two variables and the instantaneous AIRS cloud properties and ERA-Interim atmospheric and surface properties. Therefore we use in the following the input variables of experiment 4 for the model development. The 30% quantiles and 70% quantiles of the HR

315 differences in Figure S3 give an indication of the uncertainty, which may be related to differences in horizontal resolution between AIRS and CALIPSO-CloudSat. In particular for convective towers of very large optical depth (Cb) and for mid- and low-level clouds, the coarse AIRS spatial resolution may lead to a mixture of several cloud types or of clouds and clear sky within one footprint.

3.2 Sensitivity to the selection of scenes used for the training

320 The second part of sensitivity studies is dedicated to the scene types for which we develop the models: i) all clouds over the whole tropical band (one model), ii) all clouds separately over ocean and over land (two models), iii) high-level clouds and mid- / low-level clouds individually, each separately over ocean and over land (four models), and iv) Cb, Ci / thin Ci, mid- / low-level clouds individually, each separately over ocean and over land (six models). In addition, we develop models for clear sky i) over the whole tropical band (one model) and ii) separately over ocean and over land (two models). In general, a model

325 trained over all scenes together will smooth out differences between different cloud types and between ocean and land. Also scenes which are less frequent may have a smaller weight and may be therefore less represented than other scenes. Since we are interested in the study of the effect of UT cloud systems, we choose to use separate models. In particular, the modelling of Cb clouds is improved when exploiting a dedicated training for this cloud type, which represents about 7% of all clouds in the deep tropics (Stubenrauch et al., 2017).

330 When using one model for all clouds over ocean and land, the MAE is 0.82 K/day for LW and 0.51 K/day for SW HRs. Table 3 presents the MAE for the prediction of LW and SW HRs over the validation data, separately for different scene types over ocean and over land. In general, the performance is slightly better over ocean than over land, which can be explained by a greater homogeneity of surface, in particular in the SW, and atmospheric properties. We also observe a decreasing performance

from clear sky scenes (LW 0.36 K/day and SW 0.27 K/day) over mid- / low-level clouds towards high-level clouds and Cb,
335 which again can be explained by an increasing inhomogeneity, and in the case of Cb the saturation of ε_{cld} at 1.

To illustrate the effect of model aptness in dependence of training scenes, we compare in Figure 2 the difference between the
predicted radiative HRs and those from CALIPSO-CloudSat over ocean for Cb, cirrus and thin cirrus, in the LW and SW,
respectively. Compared are models which were trained i) for all clouds over ocean and land together, ii) for all clouds over
ocean, iii) for high-level clouds over ocean and iv) for Cb and for Ci / thin Ci over ocean. All results are quite similar, with the
340 differences between mean predicted and ÷observedø radiative HRs undulating well around 0 K/day. However, we observe an
overestimation of the LW cooling above Cb clouds by nearly 1 K/d when all clouds together are used to develop one single
model. The results improve for cirrus and thin cirrus when a dedicated model is developed for these cloud types. For the SW
HRs it is not possible to determine the best performance among these four models. The SW heating in the upper part of Cb
clouds is more difficult to predict, as for all four models the mean difference undulates around 0 K/day within ± 0.8 K/day
345 between 100 and 200 hPa. Considering the radiative HR profiles shown in Figure S4 of the supplement, we find that the largest
uncertainties for Cb clouds are around the maxima of LW cooling and SW heating. Furthermore, we observe that all models
give very similar results, so that in the following we will mainly use the most specific scene models, leading to the application
of eight models to reconstruct the radiative heating rate fields over the tropics.

350 **Table 3: MAE (K/d) for the prediction of LW and SW heating rates over different scene types.**

ocean	clouds	high	Cb	cirrus	mid/low	clear
LW HR	0.79	0.91	1.10	0.90	0.69	0.34
SW HR	0.45	0.62	1.10	0.59	0.33	0.22
land	clouds	high	Cb	cirrus	mid/low	clear
LW HR	0.88	0.99	1.24	0.97	0.67	0.39
SW HR	0.69	0.77	1.35	0.72	0.54	0.36

3.3 Construction of Tropical Heating Rate Fields

We then applied the ANN models to one month of AIRS data, January 2008, corresponding to a La Niña condition. During
this condition, tropical convection is shifted towards the West Pacific. In order to obtain the radiative HRs over the whole
355 tropical band, the different models were applied to the corresponding scenes. The results were then averaged at a spatial

resolution of 0.5° latitude x 0.5° longitude. This allows us to compare the results of the laterally extended radiative HRs with those of FLXHR, providing statistics only along the nadir tracks.

Figure 3 shows the contrast between the mean radiative LW and SW HRs of five cloud types (Cb, Ci, thin Ci, mid- and low-level clouds) and the one related to clear sky, as identified from AIRS, over the latitude band 30N ó 30S. For comparison, the

360 radiative HRs from FLXHR, averaged over the nadir tracks, (broken lines) are also shown. Averages of predicted and ÷observedø radiative HRs are very similar, despite different sampling and spatial resolution. This means that the nadir track statistics gives a good picture on monthly average over the whole tropics and that the prediction models provide reliable results. In a clear sky situation, LW cooling occurs, linked to the absorbed and transmitted energy by the molecules in the atmosphere. As shown in Figure 3, this cooling decreases from about -2.5 K/day with increasing height until it reaches about 0 K/day

365 around 100 hPa. Its variability over the tropics is small. Since the AIRS clear sky identification may also include subvisible cirrus as well as partly cloudy scenes within the AIRS footprint, we estimated how much this affects the radiative HRs by comparing the FLXHR HRs for AIRS clear sky and for CALIPSO-CloudSat clear sky identification. As shown in Figure S5 of the supplement, one observes a slight positive bias in the clear sky LW heating near 100 hPa of about 0.1 to 0.2 K/day due to subvisible cirrus, in particular during night, when the CALIPSO lidar better detects subvisible cirrus. The small SW clear

370 sky heating positive bias of the same order of magnitude between 400 and 800 hPa is most probably linked to contamination by partial cloudiness.

Relatively opaque clouds heat the atmospheric column below by trapping surface emissions, but cool the column above due to excess emission, while thin cirrus heat the UT by intercepting the LW radiation coming from below. Indeed, Figure 3 exhibits a LW cooling above optically thick clouds, the strongest effect above Cb, of about -4.5 K/day around 170 hPa, and a

375 heating within the clouds and below the clouds, compared to clear sky. The small cooling around 550 hPa is due to melting. The cooling above mid- and low-level clouds is located around 600 hPa and 800 hPa, respectively. Thin cirrus heat the UT around 100 hPa. In the SW range, the sunlight heats the atmosphere and the particles within the cloud. We observe a strong heating in the upper part of the Cb with a maximum of about 8 K/day around 200 hPa, while in the rest of the cloud this effect is negligible, given that the sun is blocked by the dense cloud particles. For midlevel clouds a small peak is found around 600

380 hPa and for low-level clouds around 850 hPa. The LW HRs are very similar during day and night. Although LW and SW contributions are large, their effect is opposite so that the net radiative heating during day (LW + SW) is small. This agrees very well with the expectations and earlier publications (e.g. Oreopoulos et al., 2016).

To illustrate the additional value of the lateral expansion of the radiative HRs, Figure 4 presents geographical maps of monthly mean LW heating / cooling in four specific pressure layers (around 106, 200, 525 and 850 hPa, respectively) compared to the

385 monthly mean nadir track statistics from CALIPSO-CloudSat. These four pressure layers were chosen according to 1) UT heating by thin cirrus, 2) cooling above Cb and thick cirrus, 3) middle troposphere heating by high thick clouds and 4) cooling above low-level clouds and a heating below clouds. The horizontal structures of the predicted HR fields agree quite well with

those from FLXHR, but they appear clearer, since the spare nadir track statistics is quite noisy. The comparison between the fields determined from different models in Figure S6 of the supplement gives an indication of the uncertainty, which lies

390   generally within 0.25 K/day, with a few regions of 0.45 K/day.

4 The impact of tropical UT cloud systems

By using the 3D radiative heating fields constructed in section 3, we first want to quantify the effect of clouds on the atmospheric radiative cooling, in comparison to earlier results (section 4.1). Furthermore the cloud system approach described in section 2.1 allows us to study the heating and cooling within convective cloud systems by distinguishing the HRs of the

395   convective cores (Cb), the cirrus anvil (Ci) and the surrounding thin cirrus (thin Ci). This may yield a deeper insight how the tropical heating changes with varying surface temperature (sections 4.2 and 4.3).

4.1 Tropics-wide cloud radiative heating

In general, clouds introduce sharp vertical gradients to the atmospheric radiative cooling profile, and we are in particular interested in the effect of MCSs. Li et al. (2013) have concluded that the tropics-wide 24-hr mean UT cloud radiative heating

400   effect has a narrow maximum of about 0.45 K/day around 250 hPa, and that the column-integrated radiative heating of UT clouds accounts for about 20% of the latent heating estimated by TRMM, the latter with a broad peak of about 1.7 K/day around 450 hPa. These results were obtained by using radiative heating rates calculated from ground-based lidar and radar measurements at two ARM sites (Manus and Darwin), classified by ISCCP UT cloud regimes, and then expanded over the deep tropics according to the ISCCP UT cloud regime occurrence frequency.

405   In order to compare to this significant result, we concentrate on the same latitude band from 15N to 15S and we calculate the 24-hr SW heating rates by multiplying the SW heating rates at 1:30PM LT by $1/(\pi \times \cos\Theta)$, where Θ is the solar zenith angle. The latter is about 33° near the equator. Similar to the HR normalisation of Li et al. (2013), we neglect seasonal and geographical variations. The net radiative heating is then the sum of LW and 24 hr SW heating. This estimation assumes a negligible diurnal cycle in clouds. Indeed, the diurnal cycle of UT clouds over tropical ocean is less than 2% and reaches about

410   7% over tropical land (Feofilov and Stubenrauch, 2019), with slightly less cirrus and thin cirrus at 1:30PM than at 1:30AM. This means that our estimated 24 hr net heating effect of UT clouds, thin cirrus and MCSs is slightly underestimated.
We determined the average 24 hr net radiative heating effect of specific cloud types by removing the clear sky radiative heating rate and then weighted by the total cloud cover. Figure 5 presents a tropics-wide 24 hr ó mean radiative heating induced by UT clouds throughout the troposphere, from 250 hPa downward, of about 0.3 K/day, with a broad maximum of about 0.4

415   K/day around 330 hPa and a local minimum of about 0.2 K/day around 550 hPa due to ice crystal melting at this altitude, already reported by Johannsson et al. (2015). The heating decreases towards 0 K/day at 200 hPa, and above this altitude a

small net cooling is observed. The values are in the same range as the ones determined by Li et al. (2013). However, the shape of the heating effects are significantly different: Whereas the earlier result shows a narrow maximum of 0.45 K/day around 250 hPa and a minimum heating of about 0.1 K/day around 800 hPa, our estimation indicates a much more vertically extended

420   heating, with a broader maximum of about 0.4 K/day around 330 hPa and a heating throughout the lower troposphere larger than 0.25 K/day. This then leads to a vertically different reinforcement of the latent heating, with a larger contribution between 800 hPa and 330 hPa, compared to Figure 9 of Li et al. (2013), shown in Figure S7 in the supplement. The enhancement factor between our column-integrated radiative heating of UT clouds and this latent heating (between 100 and 800 hPa) is 24%, larger than 21% found by Li et al. (2013).

425   The difference in the profile shape of the UT cloud radiative heating effect is not related to the exploitation of profiles from only two sites, as the profiles of the different cloud types, when present, averaged over both sites are similar to the ones averaged over the whole tropics (not shown). However, as discussed by Protat et al. (2014), a significant portion of the ice cloud observations using ground-based measurements is attenuated by any liquid cloud below ice clouds or by the liquid part of deep convective systems. This leads to a smaller SW heating than the satellite estimates in the middle troposphere. Another

430   key reason for an underestimation of the heating effect in the lower troposphere is that the ISCCP cloud regimes have been determined at a spatial resolution of 2.5° and especially the cirrus and mixed cloud regimes, which are the most frequent out of the four UT cloud regimes (72%), include also a certain fraction of single-layer low-level clouds next to the cirrus clouds. When considering the radiative effect of mid- and lowlevel clouds in Figure 5, which shows a cooling in the middle and lower troposphere down to 880 hPa, the shape of the radiative heating profile contribution of the ISCCP UT cloud regimes can be

435   explained by the fact that at the coarse spatial resolution of 2.5° the UT cloud regimes also contain surrounding single-layer low-level clouds. In addition, the identification of thin cirrus with optical depth less than 1.3, the most frequent within these two ISCCP cloud regimes, is also less reliable, and the cloud height in this case is often just set to the tropopause height (e. g. Stubenrauch et al., 2012).

Further consideration of Figure 5 reveals that most of the total cloud net radiative heating effect, which is the sum of the UT

440   and mid- and low-level cloud effects, comes from MCSs. The UT cooling above the opaque parts of the MCSs is compensated by thin cirrus UT heating, with half of the effect coming from those directly surrounding the anvil and the other half from in situ cirrus. The average net radiative heating within and the cooling above the MCSs seems to be slightly stronger over ocean than over land. Mid- and low-level clouds present a cooling above the clouds and a heating within and below. As there are more low-level clouds over ocean and more mid-level clouds over land, the shapes of the net heating effect differ accordingly.

445   The HR profiles of UT clouds, initially deduced from CALIPSO-CloudSat data, include the effect of lower clouds underneath, as the small warming peak around 920 hPa suggests. This peak is slightly stronger over ocean, where one expects more low-level clouds, also underneath cirrus.

From Figure 6, which compares the tropics-wide mean net radiative heating effect of the different cloud types at 1:30 AM LT and at 1:30 PM LT, we deduce a large difference in the profile shapes between nighttime and daytime, and therefore in their

450   vertical heating gradients. During nighttime, UT clouds heat the troposphere from 300 hPa downward increasingly, with a maximum of about 0.6 K/day around 920 hPa. The thicker UT clouds lead to an average cooling, with a minimum of -0.25 K/day around 200 hPa. This leads to a strong vertical gradient. The heating of the lower troposphere is slightly larger over land, but with a smaller vertical gradient in the lower troposphere. Thin cirrus have a very small average heating effect around 150 hPa, slightly larger over land than over ocean. During daytime, with additional solar heating, UT clouds, in particular the

455   thicker ones, are strongly heated (see also Figure 3), which leads to a tropics-wide maximum of about 0.6 K/day between 250 and 350 hPa. The heating strongly decreases towards the lower troposphere. Again, most of the effect of UT clouds can be explained by MCSs. The profiles reveal slightly lower but stronger systems over ocean and slightly higher systems over land, with the peak in heating located about 100 hPa higher in altitude over land than over ocean.

During nighttime and during daytime, thin cirrus have on average a small heating effect throughout the whole troposphere.

460   The effect of low-level and midlevel clouds differs diurnally: During nighttime we observe a cooling effect above these clouds, of -0.3 K/day around 820 hPa and of -0.1 K/day around 550 hPa, respectively, and a heating within and below, while during daytime the SW contribution partly compensates this effect. In general, the UT cloud effect is a strong heating of the UT during daytime and a strong lower tropospheric heating during nighttime, leading to opposite vertical gradients.

4.2 Relation between regional surface temperature and MCSs

465   A necessary condition for the onset of tropical deep convection, particularly over ocean, is a surface temperature (T_{surf}) above a threshold of about 300 K (e. g. Gray, 1968; Graham and Barnett, 1987, Aumann et al., 2018), though other factors, such as available humidity (which may increase with low-level level convergence), also affect the convective process. Though the shading of the thick anvils may cause some surface cooling during day, slightly offset by the thinner cirrus (Wall et al., 2018), MCSs should be deeper over warm regions (here defined by $T_{surf} > 302$ K) than over cool regions ($T_{surf} < 300$ K). As in a

470   changing climate the extension of warm regions may slightly increase, we compare in this section the properties of MCSs over warmer and over cooler regions.

Figure 7 presents geographical maps of UT cloud occurrence, average precipitable water and surface temperature, separately during nighttime (1:30 AM LT) and during daytime (1:30 PM LT). MCSs are most frequent over the West Pacific ocean, including Indonesia, over the Amazon region and over Central Africa. These are also the moistest regions. The West Pacific

475   region is also characterized by the warmest T_{surf} values. While over the oceanic region we do not observe a diurnal difference in UT cloud occurrence, over the two land regions UT clouds are more frequent during night, as convection starts in the early evening and cirrus anvils develop during night.

In Figure 8, distributions of the properties of maritime and continental MCSs are then compared between the warm regions and cool regions. Since the size of the MCSs may be very large (Protopapadaki et al., 2017), we only use the 50% warmest

480 underlying grid cells to determine the mean T_{surf}. In general, these warm regions are also more humid according to the distributions of precipitable water (from ERA-Interim), also shown in Figure 8. As expected, both, maritime and continental MCSs overlying warm regions have colder convective cores, which means that their convective depth is larger, and also have more often a larger horizontal extent, in agreement with a regional study by Horvath and Soden (2008), than those overlying cool regions. The area occupied by the thin cirrus surrounding their anvils is also larger for the first case. This can be explained

485 by i) a larger relative humidity at higher altitude and ii) additional UT humidification originating from the convection.
The tropics-wide 24-hr mean net radiative heating effect of the MCSs depends on their frequency, height, horizontal extent and emissivity structure. In order to study the first aspect, Figure 9 contrasts the effect of mid- / low-level clouds and UT clouds, when these are present, and also shows the resulting overall cloud effect, over cool and warm regions, respectively. Furthermore, the effects of MCSs, of the thin cirrus linked to the MCSs and of all thin cirrus are distinguished. First of all,

490 over warm regions, clouds, when present, have a heating effect over most of the troposphere, and this heating is mostly driven by MCSs. This can be seen from the fact that the profiles of the present MCSs and those of all clouds are very similar. Over cool regions mid- and in particular low-level clouds (over ocean) also play an important role, with much less heating between 200 and 900 hPa than the one of UT clouds. Over warm regions, the UT thin cirrus heating linked to convection is larger than the one of all thin cirrus, which indicates more and slightly thicker thin cirrus linked to convection than those produced in situ.

495 The influence of emissivity structure is investigated by considering the 24-hr mean net heating / cooling effects of the different parts of the MCSs, convective core (Cb), Cirrus anvil (Ci) and surrounding thin Cirrus (thin Ci), when MCSs are present. These are shown in Figure 10, for all tropical MCSs, separately over ocean and over land, and those over cool and warm regions, respectively. As already seen in Figure 3, the shape of the vertical profiles is quite different for the three parts of the MCSs. In the UT (at a height above 200 hPa), we observe an average cooling of about -2 K/day above the convective cores

500 and a less strong cooling above the cirrus anvil, while the thin cirrus heat the UT by about 0.7 K/day. The troposphere below the height of 200 hPa is strongly heated by the convective cores, much less heated by the cirrus anvils and even less by the surrounding thin cirrus. However, as the convective cores only cover a small fraction of the systems (about 10% on average), the average heating effect of the MCSs is about the one of the cirrus anvils. On average, the profiles of the three parts of the MCSs have a similar shape over ocean and over land, but the net effect of the MCSs over ocean is slightly larger than over

505 land, because the convective core fraction is smaller and the thin cirrus proportion is larger for the latter. The difference in shape of the heating profiles between cool and warm regions is larger for oceanic MCSs. For the latter, the shape of the heating profiles strengthens the hypothesis of MCSs with larger convective depth above the warm regions, with a cooling of the thicker parts of the MCSs shifted further up into the UT by 50 hPa, while the heating is extended over a broader vertical layer between

17

550 to 200 hPa. On the other hand, over both, ocean and land, the thin cirrus net radiative heating of the UT of about 0.6 K/day

510   is only connected to the deeper convective systems over the warm regions.

Gasparini et al. (2019) found that the vertical structure of the radiative heating within the anvil promotes its spreading and maintenance. The spreading then influences the heating gradients within the MCSs. To illustrate probable differences in horizontal gradients within the MCSs over cool and warm regions, we present in Figure 11 the difference of mean net radiative HR between cirrus anvil and convective cores as well as between surrounding thin cirrus and cirrus anvil, both divided by the

515   distance between these parts, assuming a system with a circular surface. This is only a very rough estimate, and to test the robustness we present averages over all MCSs and over those which have more probably a circular surface: MCSs with only one convective core and a core fraction larger than 0.05. In both cases, the 'horizontal heating / cooling gradients' within the MCSs seem to be slightly smaller in the warm regions than in the cool regions. The effects are stronger for the confirmed single core MCSs, which corroborates the quality of our data. While the horizontal effect is slightly larger over land, over

520   ocean we also observe a slight vertical shift in the horizontal gradients (Figure S12). The effect is larger in the SW and therefore larger during daytime than during nighttime (Figure S13). This difference in 'horizontal gradient' can be solely understood by the larger anvil size and therefore larger distance between the average HRs between the different parts of the MCSs, and not by a larger emissivity of the anvil and the surrounding thin cirrus, as on the contrary the average anvil emissivity is slightly smaller in the warm regions than in the cold regions (Figure S14). The latter is in agreement with a study of Del Genio et al.

525   (2005), which revealed a decreasing detrainment and increasing precipitation efficiency within maritime MCSs when the underlying T_{surf} increases.

4.3 Changes in tropical heating and in MCSs in dependence of global surface temperature anomaly

In section 4.2 we have shown that the heating in the warmer tropical regions is mostly influenced by MCSs. In this section we look at variations in MCSs and in tropical heating and try to relate these to global T_{surf} anomalies and to phenomena which

530   influence the interannual variability. The time period covered by AIRS observations may still not be long enough for climate change attribution, and in particular during most of this period global T_{surf} was quite stable. However, when comparing to linearly increasing CO_2 concentration, we perceive the T_{surf} anomalies undulating around and thus slightly increasing (Figure 12). A large attribution to the global T_{surf} anomalies, which are closely associated with tropical T_{surf} anomalies (see Figure S14 of the supplement), is given by the El-Niño-Southern Oscillation (ENSO), the most dominant mode of interannual variability

535   in the Earth's climate system. El Niño (La Niña) events are linked to a positive (negative) tropical T_{surf} anomaly. Their initiation is given by a local T_{surf} anomaly (positive T_{surf} anomaly in the equatorial eastern and central Pacific or negative T_{surf} anomaly in the tropical Pacific), changing the east-west T_{surf} gradient, which then affects the atmospheric circulation (reducing or amplifying the Walker circulation) and the distribution of clouds. However, the magnitude and also to some extent the geographical pattern of El Niño induced T_{surf} anomalies contribute to differences in cloud and circulation anomalies (e. g. Su

540   and Jiang, 2013). The Inter-decadal Pacific Oscillation (PDO), another T_{surf} anomaly in the Pacific, can be influenced by
        ENSO. The combination of both indices, the Oceanic Niño Index and the NCEI PDO index, both provided by the National
        Oceanic and Atmospheric Administration (NOAA), are therefore also presented in Figure 12.

        The average coverage of all UT cloud systems over the period 2003 to 2018 is 25.6%, with 6% from thin cirrus systems and
        80% of their coverage from MCSs. 48% of the latter are cold MCSs with T < 210 K. In order to estimate the changes in the
545   properties of the tropical MCSs in relation with global T_{surf} change, we determined the linear regression slopes between the
        anomalies of the MCS properties and the global T_{surf} anomalies. While the coverage of the MCSs is relatively stable (or very
        slightly decreasing) with warming, with -1.3 ± 0.6 %/K, the coverage of cold MCSs relative to all MCSs significantly increases
        by +18 ± 5 %/K. The latter can also be expressed by a decreasing cloud system temperature of ó 2.1 + 0.5 K/K. Furthermore,
        the surrounding thin cirrus area relative to the anvil area increases slightly by +0.041 ± 0.008 / K. The time series of 12-month
550   running means of the anomalies of the coverage of cold MCSs relative to all MCSs, of the minimum convective core
        temperature (T_{Cbmin}) and of the area of surrounding thin cirrus relative to cirrus anvil area are also shown in Figure 12. Indeed,
        they are related to global T_{surf} anomalies as well as to ENSO.

        When considering the time series of the anomalies of the vertical heating / cooling effect of the MCSs in Figure 13, we observe
        vertical dipole effects in the net during daytime, which seem to be strongly linked to ENSO variability and can be explained
555   by changes in convective depth of the MCSs. The anomalies have values of about -0.4 and +0.4 K/day, respectively. During
        La Niña periods we observe a cooling anomaly in the UT above the height corresponding to 350 hPa and a heating anomaly
        in the atmosphere below, which suggests less strong MCSs. During El Niño periods, the HR vertical structure anomaly seems
        to suggest deeper MCSs, which moves the cooling above the thick anvils and the heating within and below upward. In the LW,
        we observe a pattern of heating and cooling anomalies above the height corresponding to 200 hPa, in accordance with ENSO,
560   with more thin cirrus heating during La Niña and more thick anvil cooling during El Niño. It is interesting to note that the
        anomalies are slightly larger during nighttime.

        Zelinka and Hartmann (2010) found during El Niño periods a decrease of high-level cloud amount as well as an increase in
        their height which would have opposite effects on the OLR, with a dominating effect coming from the first. Therefore we also
        investigate the time series of heating / cooling anomalies for all clouds together in Figure 14. The anomalies in the upper and
565   middle troposphere have the same pattern as the ones for the MCSs, only much smaller, because their relative frequency of
        occurrence is taken into account. In addition, we observe strong LW cooling and heating anomaly patterns in the lower
        atmosphere, linked to the occurrence of stratocumulus and stratus cloud fields. It looks like there are more extended or thicker
        stratocumulus / stratus cloud fields when the convective systems are deeper within the latitudinal band and there are less or
        less thick when the convective systems are less deep. This confirms that height and extent of MCSs on one hand and extent of
570   the stratocumulus and stratus fields on the other are energetically constrained within the tropics and subtropics (e.g. Hang et
        al., 2019; Jakob et al., 2019).

5 Conclusions and Outlook

The active lidar and radar measurements from CALIPSO and CloudSat make it possible to derive radiative HR profiles, but only on narrow nadir tracks. On the other hand, AIRS, also part of the A-Train satellite constellation, provides cloud properties

575 with a large instantaneous horizontal coverage. By using these radiative HRs for the training and applying the resulting ANN models on cloud properties from AIRS and atmospheric and surface properties from ECMWF meteorological reanalyses, we constructed 3D HR fields within 30N to 30S, for the period 2003 to 2018.

We demonstrated that non-linear ANN regression models, trained on four years of collocated data along the nadir tracks, are appropriate methods to estimate tropical radiative HRs from about 40 cloud, atmospheric and surface properties. Column-

580 integrated MAE is about 0.8 K/day (0.5 K/day) for cloudy scenes and 0.4 K/day (0.3 K/day) for clear sky in the LW (SW). When evaluating the profile shapes, developing separate models for i) Cb, ii) cirrus and thin cirrus, iii) mid- and low-level clouds and iv) clear sky, independently over ocean and over land, leads to a small improvement, with the mean differences between predicted and ÷observedø radiative HRs well undulating around 0 K/day. The improvement is most noticeable for Cb, with uncertainties around the maxima of LW cooling and SW heating linked to slight vertical shifts between the different

585 models. The monthly mean horizontal structures of the predicted HR fields agree well with the original ones from CALIPSO-CloudSat (2B-FLXHR-LIDAR R04), but they are more obvious, due to the lateral expansion. The comparison between the fields determined from different models gives an indication of the uncertainty, which lies generally within 0.25 K/day per layer.

The input variable normalization using maximum and minimum guarantees that the regression models produce also reliable

590 results outside the training period (assuming a non-changing relationship between the input parameters and the HRs), made clear by the long-term temporal behaviour of the HRs, in particular in relation to ENSO variability.

We confirmed that most of the total cloud net radiative heating effect in the deep tropics (15N-15S) comes from UT clouds. These have a 24hr mean net radiative heating effect larger than 0.25 K/day throughout the troposphere from 250 hPa downward, with a broad maximum of about 0.4 K/day around 330 hPa, enhancing the column-integrated latent heating

595 (between 100 and 800 hPa) by 24%. This value is larger than earlier results of about 20%, using ISCCP cloud data. Our result may still be slightly underestimated, because of the not comprised diurnal variation of UT clouds, the cloud contamination of the clear sky scenes identified by AIRS and the slightly underestimated LW warming above 12 km in the original FLXHR-LIDAR (R04) data linked to cirrus microphysical assumptions. However, the shape of the heating effects compared to those of Li et al. (2013) are significantly different, with our estimation indicating a much more vertically extended heating. This

600 suggests an underestimation of the heating in the middle troposphere of the earlier result, which can be explained by the shading effect of underlying low-level clouds on ground-based measurements and by a mixture of cirrus and surrounding single-layer low-level clouds linked to the coarse spatial resolution.

Above the height corresponding to 200 hPa, the LW cooling above the opaque parts of the MCSs is compensated by thin cirrus heating, with half of the effect coming from those directly surrounding the anvil and the other half from in situ cirrus. In

605 general, the UT cloud effect is a strong heating of the UT during daytime and a strong lower tropospheric heating during nighttime, leading to opposite vertical gradients. The heating profiles also reveal slightly lower but stronger systems over ocean and slightly higher systems over land, with the peak in heating located about 100 hPa higher in altitude over land than over ocean.

The shapes of the heating profiles for the three parts of the MCSs (convective cores, cirrus anvil and surrounding thin cirrus)

610 differ significantly. The troposphere below the height of 200 hPa is strongly heated by the convective cores, much less heated by the cirrus anvils and even less by the surrounding thin cirrus. However, as the convective cores only cover a small fraction of the systems, the average heating effect of the MCSs is about the one of the cirrus anvils.

Mid- and low-level clouds produce a cooling above the clouds and a heating within and below. As there are more low-level clouds over ocean and more mid-level clouds over land, the shapes of the net heating effect differs accordingly.

615 MCSs are most frequent over the West Pacific, including Indonesia, over the Amazon region and over Central Africa. These are also the moistest regions. As expected, both, maritime and continental MCSs overlying warmer regions have colder convective cores, which means that their convective depth is larger, and the area occupied by the thin cirrus surrounding their anvils is also larger. The latter phenomenon can be explained by i) larger relative humidity at higher altitude and ii) additional UT humidification originating from the convection.

620 Over warm regions (T_{surf} > 302 K), the heating is mostly driven by MCSs, which also have a larger convective depth than the ones over cool regions (T_{surf} < 300 K). The consequence is a heating over a broader vertical layer, between 550 to 200 hPa. The thin cirrus linked to the MCSs in these regions heat the UT by about 0.7 K/day, more than the in situ formed cirrus. The latter play a more important role over cool regions, as well as mid- and low-level clouds (over ocean), with much less heating between 200 and 900 hPa.

625 The anvil spreading influences the heating gradients within the MCSs. A rough estimate of the ‑horizontal heating / cooling gradientsø within the MCSs exhibits slightly smaller ‑horizontal gradientsø in the warm regions than in the cool regions. The effect is larger in the SW and therefore larger during daytime than during nighttime. This difference in ‑horizontal gradientø can be solely understood by the larger anvil size.

During the time period 2003 to 2018, a large attribution to the global T_{surf} anomalies is given by ENSO, with El Niño (La Niña)

630 events linked to a positive (negative) T_{surf} anomaly. The time series of the anomalies of the vertical heating / cooling effect of the MCSs exhibits vertical dipole effects in the net during daytime, strongly related to ENSO variability and explained by changes in convective depth of the MCSs: During El Niño periods, the HR vertical structure anomaly suggests deeper MCS, with vertically broader heating. The LW heating and cooling anomalies above the height of 200 hPa is also in accordance with ENSO, with more thin cirrus heating during La Niña and more thick anvil cooling during El Niño. The cloud heating / cooling

21

635　anomaly patterns in the upper and middle troposphere are dominated by the MCSs, and the LW cooling / heating anomaly patterns in the lower atmosphere exhibit more stratocumulus cloud fields when there are more deep convective systems within the latitudinal band and less stratocumulus cloud fields when the MCSs are less deep. This confirms that height and amount of UT clouds on one hand and extent of the stratocumulus fields on the other are energetically constrained within the tropics and subtropics.

640　With respect to global T_{surf} anomalies, the MCS coverage is relatively stable (or very slightly decreasing) with warming, with -1.3 ± 0.6 %/K, while the coverage of cold MCSs relative to all MCSs significantly increases by +18 ± 5 %/K. Furthermore, the surrounding thin cirrus area relative to the anvil area increases slightly by +0.041 ± 0.008 / K.

In the future, we will add the latent heating profiles derived from the Tropical Rainfall Measuring Mission (TRMM) to this synergistic data set, which provides for the first time a 3D view of the radiative heating profiles over a long time period,. As

645　the coincidences in time with AIRS are small, we will use again machine learning techniques, similar to the ones described in this article. This data base of UT cloud systems is being constructed within the framework of the GEWEX (Global Energy and Water Exchanges) Process Evaluation Study on Upper Tropospheric Clouds and Convection (GEWEX UTCC PROES, https://gewex-utcc-proes.aeris-data.fr/) to advance our knowledge on the climate feedbacks of UT clouds. In general, climate feedback studies are undertaken by climate model simulations, which rely upon their representation of convection and

650　detrainment. The cloud system approach has already proved its usefulness in the evaluation of a new bulk ice cloud scheme in the LMD GCM (Stubenrauch et al., 2019), and the HRs may be used to distinguish between parameterizations of ice cloud radiative properties. Furthermore, this data base, in particular when including the total 3D diabatic heating, will be used to quantify the dynamical response of the climate system to the atmospheric heating induced by the anvil cirrus, refining and extending the studies of Schumacher et al.(2004) and Li et al. (2013).

References

665   Ackerman, T. P., Liou, K.-N., Valero, F. P. J., and Pfister, L.: Heating Rates in Tropical Anvils, J. Atmos. Sci., 45, 1606-1623, https://doi.org/ 10.1175/1520-0469(1988)045<1606:HRITA>2.0.CO;2, 1988.

Aumann, H. H., Behrangi, A., and Wang, Y.: Increased Frequency of Extreme Tropical Deep Convection: AIRS Observations and Climate Model Predictions, Geophys. Res. Lett., 45, 13530-13537, https://doi.org/10.1029/2018GL079423, 2018.

Bergman, J. W., and Hendon, H. H.: Cloud Radiative Forcing of the Low-Latitude Tropospheric Circulation: Linear
670   Calculations, J. Atmos. Sci., 57, 2225-2245, https://doi.org/10.1175/1520-0469(2000)057<2225:CRFOTL>2.0.CO;2, 2000.

Boucher, O., D. Randall, P. Artaxo, C. Bretherton, G. Feingold, P. Forster, V.-M. Kerminen, Y. Kondo, H. Liao, U. Lohmann, P. Rasch, S.K. Satheesh, S. Sherwood, B. Stevens, and X.Y. Zhang, Clouds and aerosols. In Climate Change 2013: The Physical Science Basis. Contribution of Working Group I to the Fifth Assessment Report of the Intergovernmental Panel on Climate Change. T.F. Stocker, D. Qin, G.-K. Plattner, M. Tignor, S.K. Allen, J. Doschung, A. Nauels, Y. Xia, V. Bex, and
675   P.M. Midgley, Eds. Cambridge University Press, 571-657, https://doi.org/10.1017/CBO9781107415324.01, 2013.

Chahine, M. T., Pagano, T. S., Aumann, H. H., Atlas, R., Barnet, C., Blaisdell, J., Chen, L., Divakarla, M., Fetzer, E. J., Goldberg, M., Gautier, C., Granger, S., Hannon, S., Irion, F. W., Kakar, R., Kalnay, E., Lambrigtsen, B. H., Lee, S., Le Marshall, J., McMillan, W. W., McMillin, L., Olsen, E. T., Revercomb, H., Rosenkranz, P., Smith,W. L., Staelin, D., Strow, L. L., Susskind, J., Tobin, D., Wolf, W., and Zhou, L.: AIRS: Improving weather forecasting and providing new data on
680   greenhouse gases, Bull. Amer. Meteor. Soc., 87, 911-926, https://doi.org/10.1175/BAMS-87-7-911, 2006.

Chédin, A., Scott, N. A., Wahiche, C., and Moulinier, P.: The improved initialization inversion method: A high resolution physical method for temperature retrievals from satellites of the TIROS-N series, J. Climate Appl. Meteor., 24, 128-143, https://doi.org/10.1175/1520-0450(1985)024%3C0128:TIIIMA%3E2.0.CO;2, 1985.

Chédin, A., Serrar, S., Scott, N. A., Crevoisier, C., and Armante, R.: First global measurement of midtropospheric CO_2 from
685   NOAA polar satellites: Tropical zone, J. Geophys. Res., 108, https://doi.org/101029/2003JD003439, 2003.

Dee, D. P., Uppala, S. M., Simmons, A. J., Berrisford, P., Poli, P., Kobayashi, S., Andrae, U., Balmaseda, M. A., Balsamo, G., Bauer, P., Bechtold, P., Beljaars, A. C. M., van de Berg, L., Bidlot, J., Bormann, N., Delsol, C., Dragani, R., Fuentes, M., Geer, A. J., Haimberger, L., Healy, S. B., Hersbach, H., Holm, E. V., Isaksen, L., Kallberg, P., Kohler, M., Matricardi, M., McNally, A. P., Monge-Sanz, B. M., Morcrette, J.-J., Park, B.-K., Peubey, C., de Rosnay, P., Tavolato, C., Thepaut, J.-N., and
690   Vitart, F.: The ERA-Interim reanalysis: configuration and performance of the data assimilation system, Q. J. R. Meteorol. Soc., 137, 553ó597, https://doi.org/10.1002/qj.828, 2011.

Del Genio, A.D., W. Kovari, M.-S. Yao, and J. Jonas: Cumulus microphysics and climate sensitivity. *J. Climate*, 18, 2376-2387, https://doi.org/10.1175/JCLI3413.1, 2005.

Deng M, Mace, G. G., Wang, Z., and Lawson, R. P.: Evaluation of Several A-Train Ice Cloud Retrieval Products with In Situ

695   Measurements Collected during the SPARTICUS Campaign. J. Appl. Meteor. Climatol., 52, 1014ó1030, https://doi.org/10.1175/JAMC-D-12-054.1, 2013.

Ham, S.-H., Kato, S., Rose, F. G., Winker, D., LøEcuyer, T., Mace, G. G., Painemal, D., Sun-Mack, S, Chen, Y., and Miller W. F.: Cloud occurrences and cloudradiative effects (CREs) fromCERES-CALIPSO-CloudSat-MODIS (CCCM) and CloudSat radar-lidar (RL) products, J. Geophys. Res. Atmos., 122, 8852ó8884, https://doi.org/10.1002/2017JD026725, 2017.

700   Feofilov, A. G., Stubenrauch, C. J., and Delanoë, J.: Ice water content vertical profiles of high-level clouds: classification and impact on radiative fluxes, Atmos. Chem. Phys., 15, 12327ó12344, https://doi.org/10.5194/acp-15-12327-2015, 2015.

Feofilov, A. G. and Stubenrauch, C. J., Diurnal variation of high-level clouds from the synergy of AIRS and IASI space-borne infrared sounders, Atmos. Chem. Phys., 19, 13957-13972, https://doi.org/10.5194/acp-19-13957-2019, 2019.

Gasparini, B., Blossey, P. N., Hartmann, D. L., Lin, G., and Fan, J.: What drives the life cycle of tropical anvil clouds? J.

705   Advances in Modeling Earth Systems, 11, 2586ó 2605. https://doi.org/10.1029/2019MS001736, 2019.

Guignard, A., Stubenrauch, C. J., Baran, A. J., and Armante, R.: Bulk microphysical properties of semi-transparent cirrus from AIRS: a six year global climatology and statistical analysis in synergy with geometrical profiling data from CloudSat-CALIPSO, Atmos. Chem. Phys., 12, 503ó525, https://doi.org/10.5194/acp-12-503-2012, 2012.

Graham, N. E., and Barnett, T. P.: Sea Surface Temperature, Surface Wind Divergence, and Convection over Tropical Oceans,

710   Science, 238(4827):657-9, https//doi.org/10.1126/science.238.4827.657, 1987.

Gray, W.: A global view of the origin of tropical disturbances and storms, Mon. Weath. Rev., 96, 669-700, https://doi.org/10.1175/1520-0493(1968)096<0669:GVOTOO>2.0.CO;2, 1968.

Hang, Y., LøEcuyer, T. S., Henderson, D. S., Matus, A. V., and Wang, Z.: Reassessing the Effect of Cloud Type on Earthøs Energy Balance in the Age of Active Spaceborne Observations. Part II: Atmospheric Heating. J. Climate, 32, 6219ó6236,

715   https://doi.org/10.1175/JCLI-D-18-0754.1, 2019.

Haynes, J. M., LøEcuyer, T., Stephens, G. L., Miller, S. D., Mitrescu, C., Wood, N. B., and Tanelli, S.: Rainfall retrieval over the ocean with spacenorne W-band radar, J. Geophys. Res. Atmospheres, 114, D00A22, https://doi.org/10.1029/2008JD009973, 2009.

Henderson, D. S., LøEcuyer, T., Stephens, G. L, Partain, P., and Sekiguchi, M.: A Multisensor Perspective on the Radiative

720   Impacts of Clouds and Aerosols, J. Appl. Meteor. Climatol., 52, 853ó871, https://doi.org/10.1175/JAMC-D-12-025.1, 2013.

Hersbach, H., and coauthors: The ERA5 Global Reanalysis, Quarterly J. Roy. Meteor. Soc., https://doi.org/10.1002/qj.3803, 2020.

Horvath, A., and Soden, B. J., Lagrangian diagnostics of tropical deep convection and its effect upon upper-tropospheric humidity. J. Climate, 21, 1013-1028. https://doi.org/10.1175/2007JCLI1786.1, 2008.

725   Houze, R. A. Jr., Mesoscale convective systems, Rev. Geophys., 42, RG4003, https://doi.org/10.1029/2004RG000150, 2004.

Hsieh, W. W.: Machine Learning Methods in the Environmental Sciences: Neural Networks and Kernels, Cambridge University Press, 2009.

Igel, M. R., Drager, A. J., and Van Den Heever, S. C.: A CloudSat cloud object partitioning technique and assessment and integration of deep convective anvil sensitivities to sea surface temperature, J. Geophys. Res., 119, 10515-10535, https://doi.org/10.1002/2014JD021717, 2014.

Jakob, C., Singh, M. S., and Jungandreas, L.: Radiative convective equilibrium and organized convection: An observational perspective. J. Geophys. Res. Atmospheres, 124, 5418ó5430. https://doi.org/10.1029/2018JD030092, 2019.

Johansson, E., Devasthale, A., L'Ecuyer, T., Ekman, A. M. L., and Tjernström, M.: The vertical structure of cloud radiative heating over the Indian subcontinent during summer monsoon, Atmos. Chem. Phys., 15, 11557ó11570, https://doi.org/10.5194/acp-15-11557-2015, 2015.

Kingma, D. P., and Ba, J., Adam: A Method for Stochastic Optimization, 3rd Int. Conf. for Learning Representations, San, Diego, 2015, arXiv: 1412.6980, 2014.

Kleynhans, T., Montanaro, M., Gerace, A., and Kanan, C.: Predicting Top-of-Atmosphere Thermal Radiance Using MERRA-2 Atmospheric Data with Deep Learning. Remote Sens., 9, 1133, https://doi.org/10.3390/rs9111133, 2017.

Lenssen, N., Schmidt, G., Hansen, J., Menne, M., Persin, A., Ruedy, R., and Zyss, D., Improvements in the GISTEMP uncertainty model. J. Geophys. Res. Atmos., 124, 12, 6307-6326, https://doi.org/10.1029/2018JD029522, 2019.

Levy, R., Remer, L., Tanré, D., Mattoo, S., and Kaufman, Y.: Algorithm for remote sensing of tropospheric aerosol over dark targets from MODIS: Collections 005 and 051: Revision 2, MODIS Algorithm Theoretical Basis Document, 2009.Roca, R., Aublanc, J., Chambon, P., Fiolleau, T., and Viltard, N.: Robust Observational Quantification of the Contribution of Mesoscale Convective Systems to Rainfall in the Tropics. J. Climate, 27, 495ó4958, https://doi.org/10.1175/JCLI-D-13-00628.1, 2014.

Li, W., Schumacher, C., and McFarlane, S. A.: Radiative heating of the ISCCP upper level cloud regimes and its impact on the large-scale tropical circulation, J. Geophys. Res. Atmos., 118, 592ó604, https://doi.org/10.1002/jgrd.50114, 2013.

Luo, Z., and Rossow, W.B.: Characterizing tropical cirrus life cycle, evolution, and interaction with upper-tropospheric water vapor using Lagrangian trajectory analysis of satellite observations. J. Climate, 17, 4541-4563, https://doi.org/10.1175/3222.1, 2004.

Mace, G. G., Zhang, Q., Vaughan, M., Marchand, R., Stephens, G., Trepte, C., and Winker, D.: A description of hydrometeor layer occurrence statistics derived from the first year of merged Cloudsat and CALIPSO data, J. Geophys. Res., 114, D00A26, https://doi.org/10.1029/2007JD009755, 2009.

Matus, A. ,and LEcuyer, T.S.: The role of cloud phase in Earthøs radiation budget. J. Geophys. Res. Atmos., 122, 2559-2578, https://doi.org/10.1002/2016JD025951, 2017.

Oreopoulos, L., Cho, N., Lee, D., and Kato, S.: Radiative effects of global MODIS cloud regimes, J. Geophys. Res. Atmos., 121, 2299ó2317, https://doi.org/10.1002/2015JD024502, 2016.

Paul, M., Aires, F., Prigent, C., Trigo, I., and Bernardo, F.: An innovative physical scheme to retrieve simultaneously surface temperature and emissivities using high spectral infrared observations from IASI. J. Geophys. Res., 117, D11302, https://doi.org/10.1029/2011JD017296, 2012.

760 Protat, A., Young, S.A. McFarlane, S.A., LøEcuyer, T., Mace, G.G., Comstock, J.M., Long, C.N., Berry, E., and Delanoë, J.: Reconciling Ground-Based and Space-Based Estimates of the Frequency of Occurrence and Radiative Effect of Clouds around Darwin, Australia, J. Appl. Meteor. Climatol., 53, 456ɓ478, https://doi.org/10.1175/JAMC-D-13-072.1, 2014.

Protopapadaki, E.-S., Stubenrauch, C. J., and Feofilov, A. G.: Upper Tropospheric cloud Systems derived from IR Sounders:
765 Properties of Cirrus Anvils in the Tropics, Atmosph. Chem. Phys., 17, 3845-3859, https://doi.org/10.5194/acp-17-3845-2017, 2017.

Reichler, T., Dameris, M., and Sausen, R.: Determining the tropopause height from gridded data, Geophys. Res. Lett., 30, 2042, https://doi.org/10.1029/2003GL018240, 2003.

Ritter, B., and Geleyn, J.-F.: A comprehensive radiation scheme for numerical weather prediction models with potential
770 applications in climate simulations. Mon. Wea. Rev., 120, 303ɓ325, https://doi.org/10.1175/1520-0493(1992)120<0303:ACRSFN>2.0.CO;2, 1992.

Schumacher, C., Houze, R. A., and Kraucunas, I., The Tropical Dynamical Response to Latent Heating Estimates Derived from the TRMM Precipitation Radar, J. Atmos. Sci., 61, 1341-1358, https://doi.org/10.1175/1520-0469(2004)061<1341 :TTDRTL>2.0.CO;2, 2004.

775 Sherwood, S. C., Ramanathan, V., Barnett, T., Tyree, M., and Roeckner, E.: Response of an atmospheric GCM to radiative forcing of tropical clouds. J. Geophys. Res., 99, 20 829ɓ20 845, https://doi.org/10.1002/qj.49711448209, 1994.

Slingo, J. M., and Slingo, A.: The response of a general circulation model to cloud longwave radiative forcing. II: Further studies, Quart. J. Roy. Meteor. Soc., 117, 333ɓ364, https://doi.org/10.1002/qj.49711448209, 1991.

Snauffer, A. M., Hsieh, W. W., Cannon, A. J., and Schnorbus, M. A.: Improving gridded snow water equivalent products in
780 British Columbia, Canada: multi-source data fusion by neural network models, The Cryosphere, 12, 891-905, https://doi.org/10.5194/tc-12-891-2018, 2018.

Sohn, B.-J.: Cloud-Induced Infrared Radiative Heating and Its Implications for Large-Scale Tropical Circulations, J. Atmos. Sci., 56, 2657-2672, https://doi.org/10.1175/1520-0469(1999)056<2657:CIIRHA>2.0.CO;2, 1999.

Stein, T. H. M., Holloway, C. E., Tobin, I., and Bony, S.: Observed relationships between cloud vertical structure and
785 convective aggregation over tropical ocean. J. Climate, 30, 2187ɓ2207, https://doi.org/10.1175/JCLI-D-16-0125.1, 2017.

Stephens, G. L., and Webster, P. J. : Cloud decoupling of surface and planetary radiative budgets. J. Atmos. Sci., 41, 681ɓ686, https://doi.org/ 10.1175/1520-0469(1984)041<0681:CDOTSA>2.0.CO;2, 1984.

Stephens, G. L., Vane, D. G, .Boain, R. J., Mace, G. G., Sassen, K., Wang, Z., Illingworth, A. J., OɸConnor, E. J., Rossow, W.

26

B., Durden, S. L., Miller, S. D., Austin, R. T., Benedetti, A., Mitrescu, C., and CloudSat Science Team: The CloudSat mission and the A-Train: A new dimension of space-based observations of clouds and precipitation. Bull. Amer. Meteorol. Soc., 83, 1771-1790, https://doi.org/10.1175/BAMS-83-12-1771, 2002.

Stephens, G. L, Van den Heever, S., and Pakula, L. A.: Radiative Convective Feedback in Idealized States of Radiative-Convective Equilibrium. J. Atmos. Sci., 65, 3899-3916, https://doi.org/10.1175/2008JAS2524.1, 2008.

Strahler, A. H., Muller, J.-P., and MODIS Science Team Members: MODIS BRDF/Albedo Product: Algorithm Theoretical Basis Document Version 5.0, MODIS Product ID: ATBD-MOD-43, 1999.

Stubenrauch, C. J., Chédin, A., Armante, R. and Scott, N. A.: Clouds as Seen by Satellite Sounders (3I) and Imagers (ISCCP): II) A New Approach for Cloud Parameter Determination in the 3I Algorithms, J. Climate, 12, 2214-2223, https://doi.org/10.1175/1520-0442(1999)012<2214:CASBSS>2.0.CO;2, 1999.

Stubenrauch, C. J., Rossow, W. B., Kinne, S., Ackerman, S., Cesana, G., Chepfer, H., Di Girolamo, L., Getzewich, B., Guignard, A., Heidinger, A., Maddux, B., Menzel, P., Minnis, P., Pearl, C., Platnick, S., Poulsen, C., Riedi, J., Sun-Mack, S., Walther, A., Winker, D., Zeng, S., Zhao, G.: Assessment of Global Cloud Datasets from Satellites: Project and Database initiated by the GEWEX Radiation Panel, Bull. Amer. Meteor. Soc., https://doi.org/10.1175/BAMS-D-12-00117.1, 2013.

Stubenrauch, C. J., Feofilov, A. G., Protopapadaki, E.-S., & Armante, R.: Cloud climatologies from the InfraRed Sounders AIRS and IASI: Strengths and Applications, Atmosph. Chem. Phys., 17, 13625-13644, https://doi.org/10.5194/acp-17-13625-2017, 2017.

Stubenrauch, C. J., Bonazzola, M., Protopapadaki, S. E., and Musat, I., New cloud system metrics to assess bulk ice cloud schemes in a GCM. J. Advances in Modeling Earth Systems, 11, https://doi.org/10.1029/2019MS001642, 2019.

Su, H., and Jiang, J. H., Tropical Clouds and Circulation Changes During the 2006-07 and 2009-10 El Niños, J. Climate, 26, 3996413, https://doi.org/10.1175/JCLI-D-12-00152.1, 2013.

Tan, J., Jakob, C., Rossow, W.B. and Tselioudis, G.: The role of organized deep convection in explaining observed tropical rainfall changes. Nature, 519, 451-454, https://doi.org/10.1038/nature14339, 2015.

Trepte, Q. Z., Minnis, P., Trepte, C. R., Sun-Mack, S., and Brown, R.: Improved cloud detection in CERES Edition 3 algorithm and comparison with the CALIPSO Vertical Feature Mask. Proc. 13th Conf. on Atmosph. Radiation and Cloud Physics, Portland, Amer. Meteor. Soc., JP1.32, (https://ams.confex.com/ams/13CldPhy13AtRad/webprogram/Paper171785.html), 2010.

Tselioudis, G., Rossow, W. B., Zhang, Y., and Konsta, D.: Global Weather States and Their Properties from Passive and Active Satellite Cloud Retrievals, J. Climate, 26, 7734-7746, https://doi.org/10.1175/JCLI-D-13-00024.1, 2013.

Wall, C. J., Hartmann, D. L., Thieman, M. M., Smith, W. L., and Minnis, P.: The life cycle of anvil clouds and the top-of-atmosphere radiation balance over the tropical West Pacific. J. Climate, 31, 10,0596 10,080. https://doi.org/10.1175/JCLI-D-18-0154.1, 2018.

Winker, D. M., Vaughan, M. A., Omar, A., Hu, Y., and Powell, K. A.: Overview of the CALIPSO mission and CALIOP data processing algorithms, J. Atmos. Oceanic. Technol., 26, 2310-2323, https://doi.org/10.1175/2009JTECHA1281.1, 2009.

Wu, X. and Smith, W. L.: Emissivity of rough sea surface for 8⎼13 m: modelling and verification, Appl. Optics, 36, 2609⎼2619, https://doi.org/10.1364/AO.36.002609, 1997.

825 Yuan, J., and Houze Jr, R. A.: Global Variability of Mesoscale Convective System Anvil Structure from A-Train Satellite Data, J. Climate, 23, 5864-5888, https://doi.org/10.1175/2010JCLI3671.1, 2010.

Zelinka, M. D., and Hartmann, D. L.: Why is longwave cloud feedback positive?, J. Geophys. Res., 115, D16117, https://doi.org/10.1029/2010JD013817, 2010.

Zelinka, M. D., Zhou, C., and Klein, S. A.: Insights from a refined decomposition of cloud feedbacks, Geophys. Res. Lett., 43, 830 9259-9269, https://doi.org/10.1002/2016GL069917, 2016.
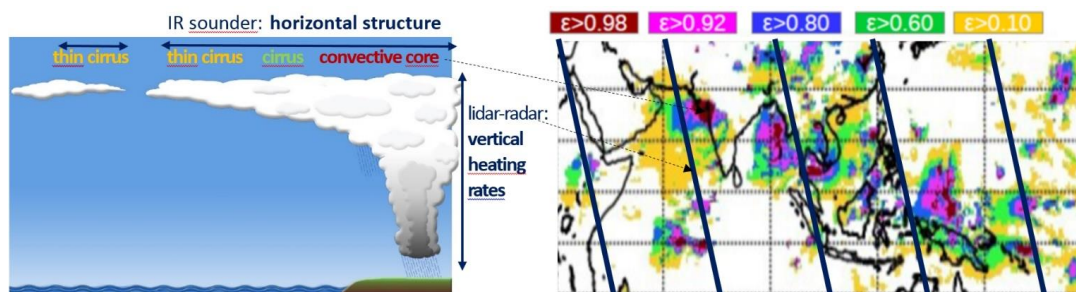
Figures

Figure 1: Illustration of three dimensional Cloud System Concept, using spaceborne IR Sounder data (AIRS), providing the horizontal component, and lidar-radar data (CALIPSO-CloudSat), providing the vertical component, both part of NASA's A-Train satellite constellation (left): Based on two independent variables retrieved by AIRS, UT cloud systems are reconstructed from adjacent elements of similar cloud height (p_{cld}), the horizontal emissivity structure allows to directly link the properties of convective cores ($\varepsilon_{cld} > 0.98$) and cirrus anvils (right). Clear sky and low-level cloud fields are also identified (Fig. 4a of Protopapadaki et al. 2017). A horizontally complete picture of the vertical radiative heating rates will be obtained by laterally expanding them, as they are only available along narrow lidar-radar tracks (dark blue). Therefore we have developed optimized "non-linear regression models", using deep neural network learning techniques, described in section 2.5 and evaluated in section 3, to relate the most suitable cloud and atmospheric properties from IR sounder and meteorological reanalyses to these heating rates.
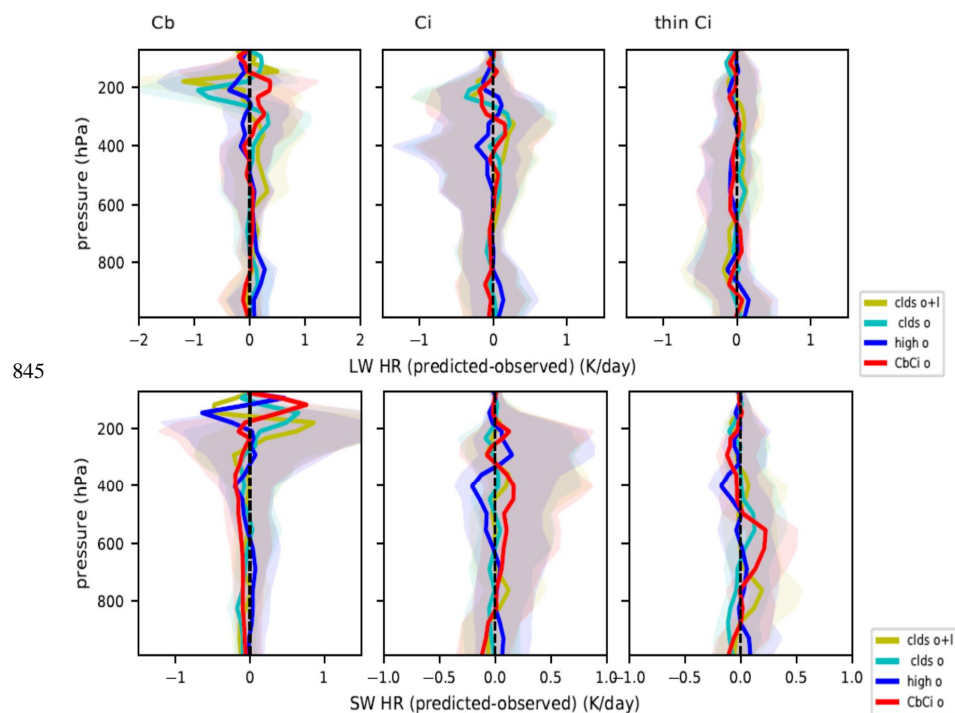
845

850

Figure 2: Sensitivity results concerning training over different scenes (high clouds over ocean, all clouds over ocean and all clouds over ocean and land) for the prediction of high-level cloud LW radiative heating rates (above) and SW radiative heating rates (below): difference between predicted and observed vertical profiles, separately for Cb, Cirrus and thin Cirrus, as identified by AIRS-CIRS, over tropical ocean. 30% and 70% quantiles of the distributions are also shown.
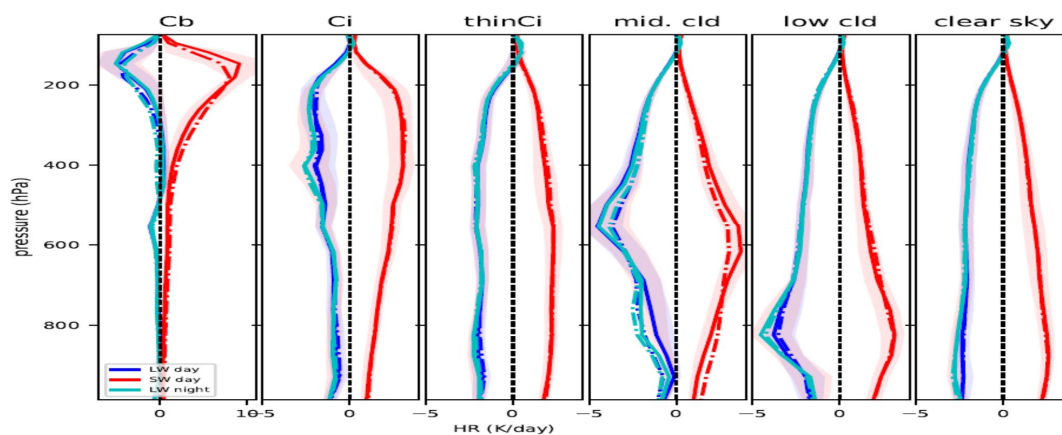
Figure 3: Predicted LW heating rates and SW heating rates (full line), separately for Cb, Cirrus, thin Cirrus, mid-and low-level clouds and clear sky, as identified by AIRS-CIRS, averaged over the AIRS swaths within 30N ó 30S, in January 2008. 30% and 70% quantiles of the distributions indicate their variability. The model has been trained individually over Cb, Ci / thin Ci and mid- / low-
855 **level clouds, separately over ocean and land. Broken lines correspond to the average of FLXHR heating rates averaged along the CALIPSO-CloudSat nadir tracks. Night corresponds to 1:30 AM and day to 1:30 PM local time.**
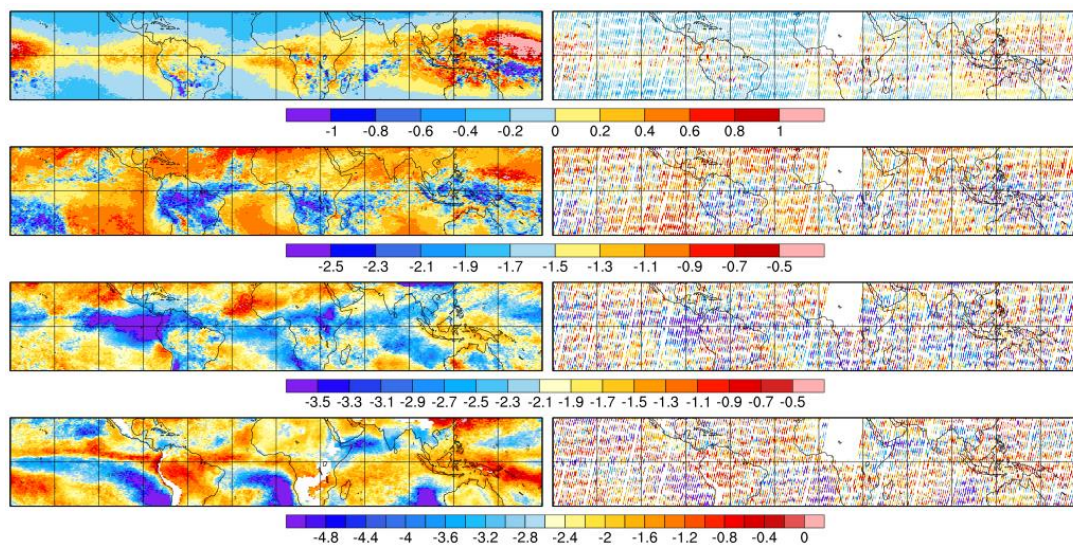
860

Figure 4: Geographical maps of LW heating rates (K/day) in 4 layers: 106-131 hPa, 200-223 hPa, 525 ó 585 hPa and 850 ó 900 hPa (from top to bottom) averaged over January 2008 at 1:30AM. Left: predicted over the AIRS swath, using the combination of the eight models developed for Cb, Ci / thin Ci, mid- / low-level clouds and clear sky, separately over ocean and over land. Right: from
865 **NASA FLXHR data along the CALIPSO-CloudSat nadir tracks.**
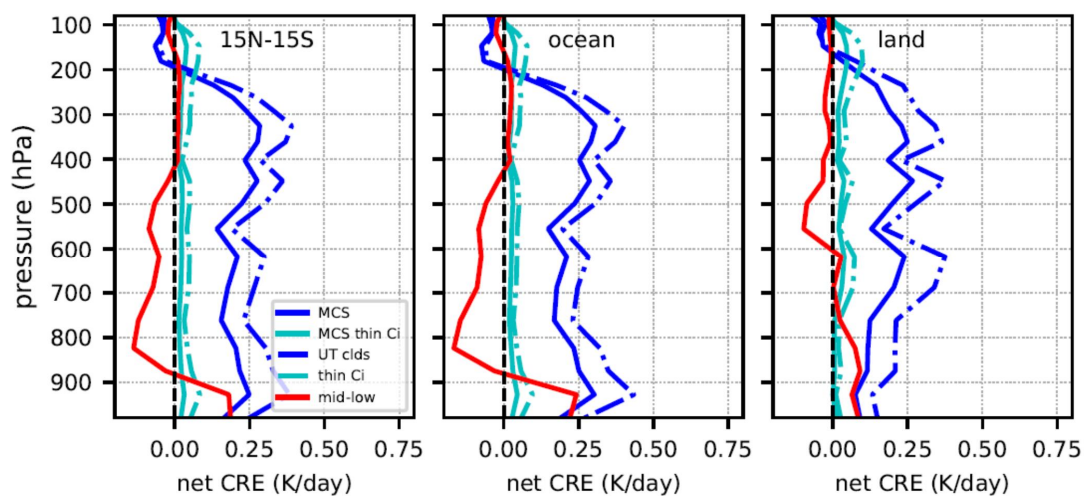
Figure 5: Tropical mean net radiative heating effect within the troposphere of low- and mid-level clouds (red) and UT clouds (blue, broken line), for the latter the effect of MCSs (blue), thin cirrus surrounding MCSs (cyan, full line) and all thin cirrus (cyan, broken line) is shown separately. Left: all, middle: ocean, right: land. Cloud observations at 1:30PM local time, with SW radiation normalized to 24 hours, similar to Li et al. (2013). Statistics of 15 years (2004 ó 2018), averaged over 15N to 15S. The sum of UT cloud and mid- / lowlevel cloud contributions corresponds to the total cloud heating effect, defined as the difference between total and clear sky heating.

33
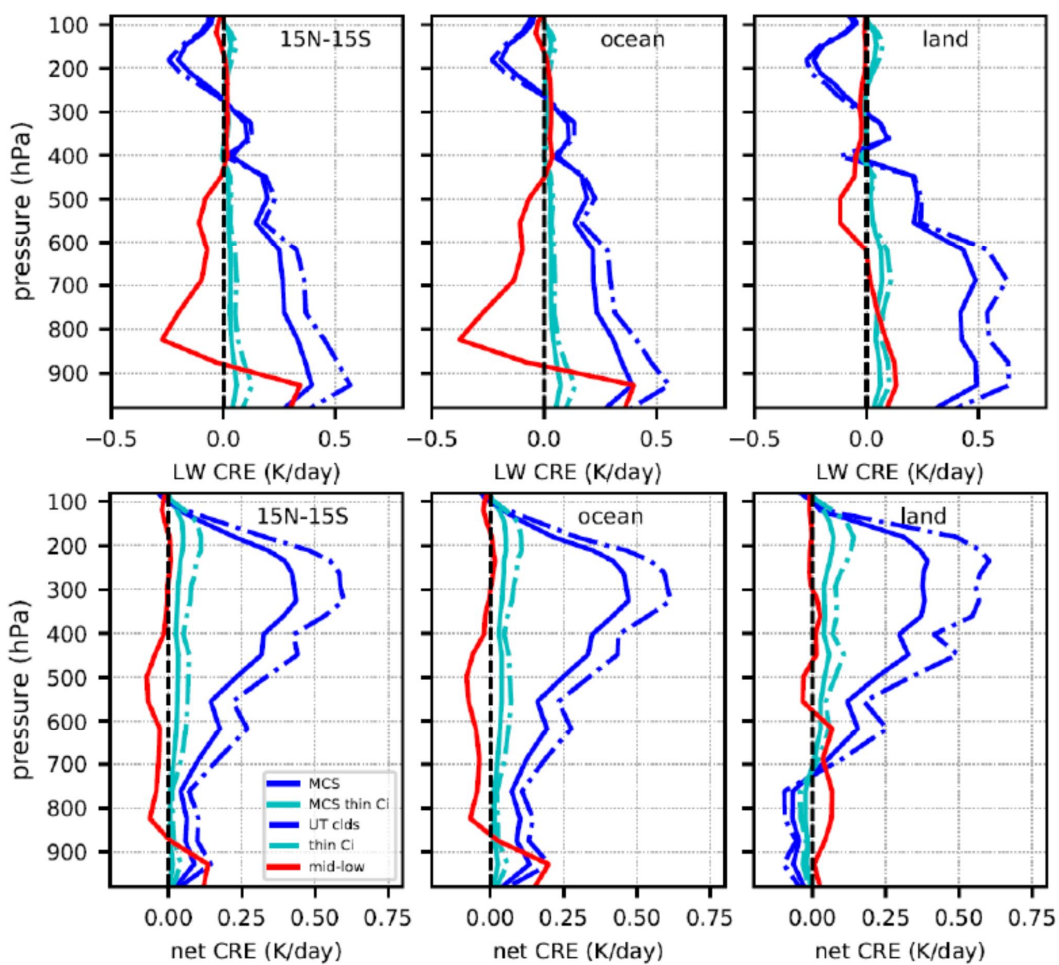
Figure 6: Tropical mean net radiative heating effect within the troposphere of low- and mid-level clouds (red) and UT clouds (blue, broken line), for the latter the effect of MCSs (blue), thin cirrus surrounding MCSs (cyan, full line) and all thin cirrus (cyan, broken line) is shown separately. Left: all, middle: ocean, right: land. Above: at 1:30AM local time, below: at 1:30PM local time. Statistics of 15 years (2004 ó 2018), averaged over 15N to 15S.
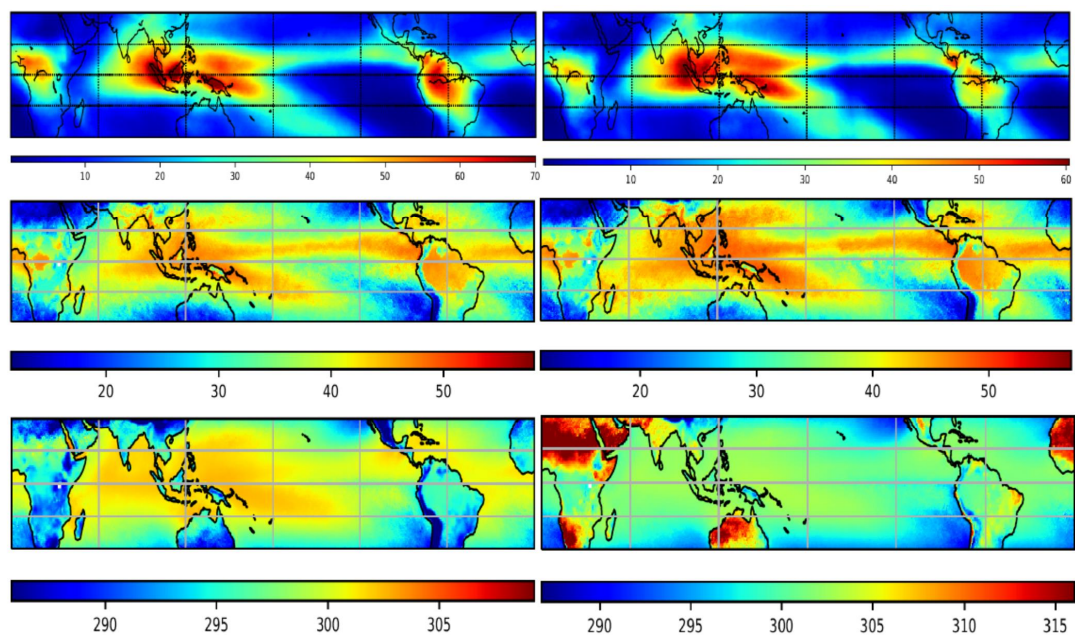
Figure 7: Geographical maps of occurrence frequency of UT clouds (top row), of total precipitable water in mm (middle row) and of surface temperature in K (bottom row), at 1:30 AM LT (left) and at 1:30 PM LT (right). Statistics of 16 years (2003-2018).
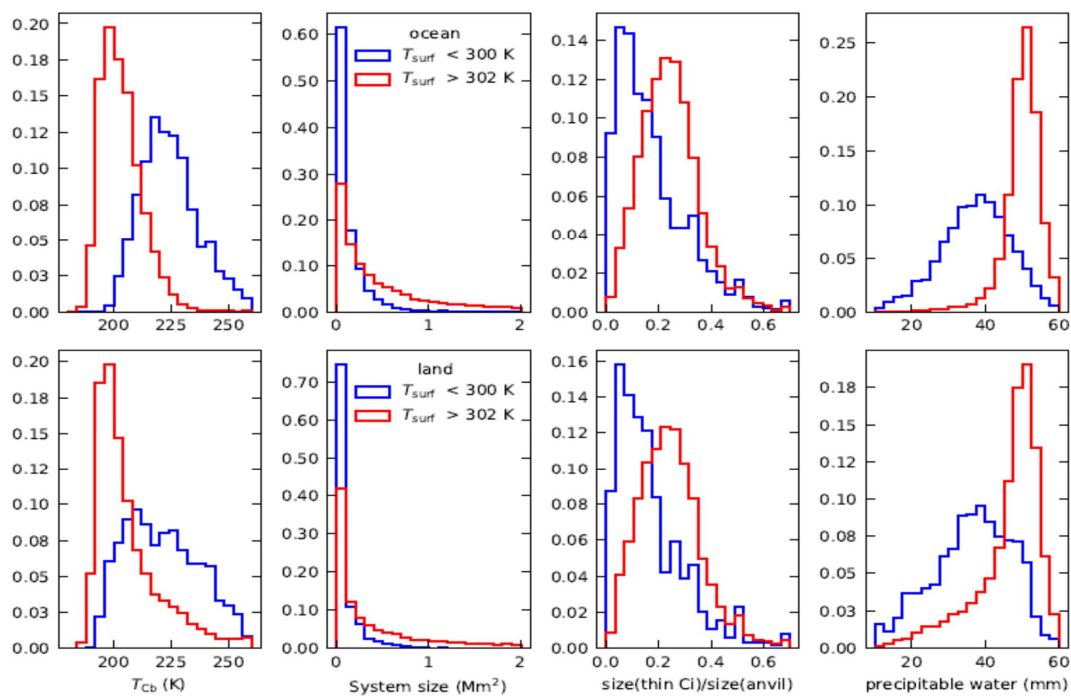
890 **Figure 8: Normalized distributions of properties of the tropical MCSs (temperature of convective core, cloud system size, relative size of the thin cirrus within or surrounding the anvil) and atmospheric precipitable water, separately for systems with a smaller and a larger underlying surface temperature, over ocean (above) and over land (below), at 1:30 PM LT.**
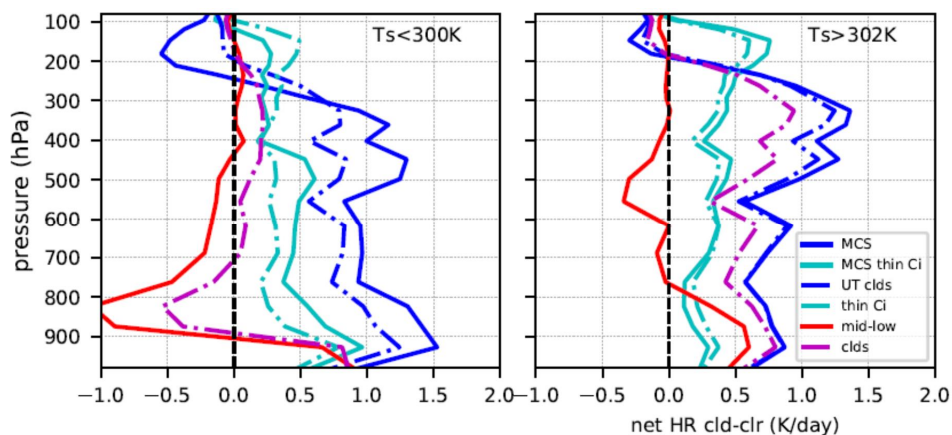
Figure 9: Tropical 24-hour mean cloud net radiative heating effect (magenta) within the troposphere, and separately the effect of low- and mid-level clouds (red), mesoscale convective systems (blue), thin cirrus (cyan) and all UT cloud systems (black), averaged over 15N to 15S, when clouds or the specific cloud types are present. Left: regions with $T_{surf} < 300$ K, right: regions with $T_{surf} > 302$ K.

Atmospheric
Chemistry
and Physics
Discussions

Open Access

EGU
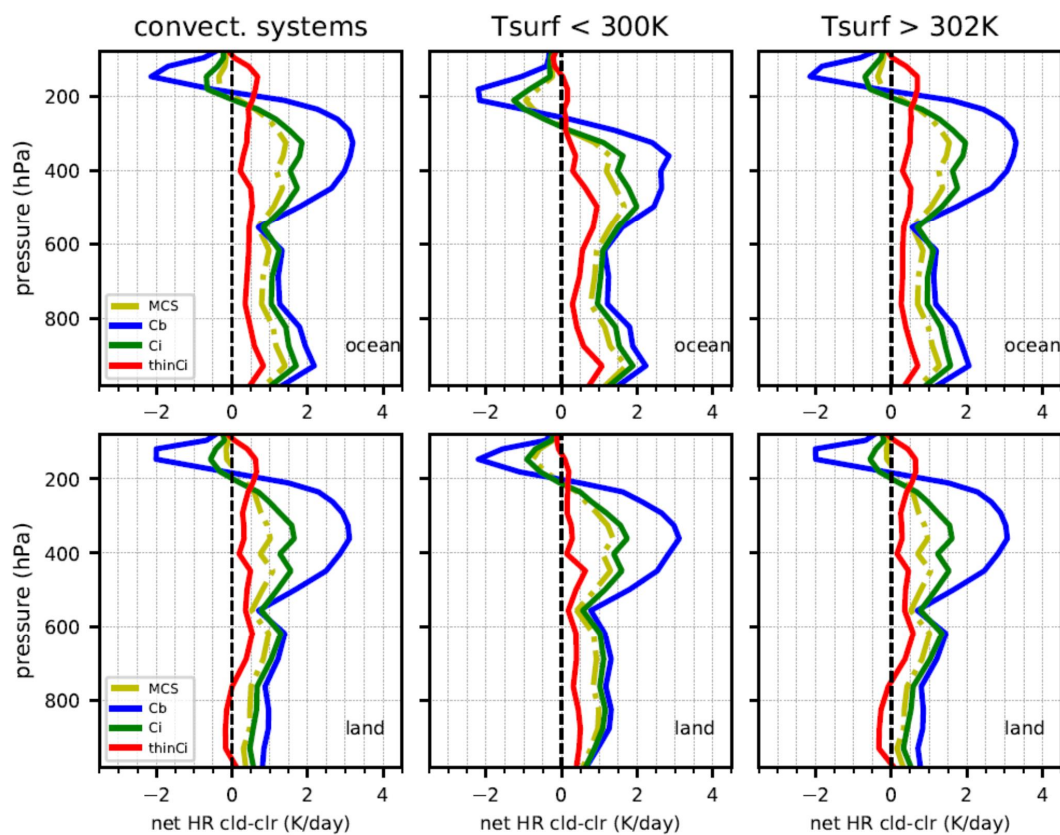
Figure 10: Mean net radiative heating effect of MCSs, when present, and their convective cores (Cb), cirrus anvil (Ci) and surrounding thin cirrus (thinCi) over ocean (top) and over land (with $p_{surf} > 900$ hPa, bottom), at 1:30 AM local time. In addition, MCSs with the 25% warmest areas of $T_{surf} < 300$K and of $T_{surf} > 302$K are distinguished (from left to right). Cloud observations at 1:30PM local time, with SW radiation normalized to 24 hours. Statistics of 15 years (2004-2018), averaged over 15N to 15S.

900

905
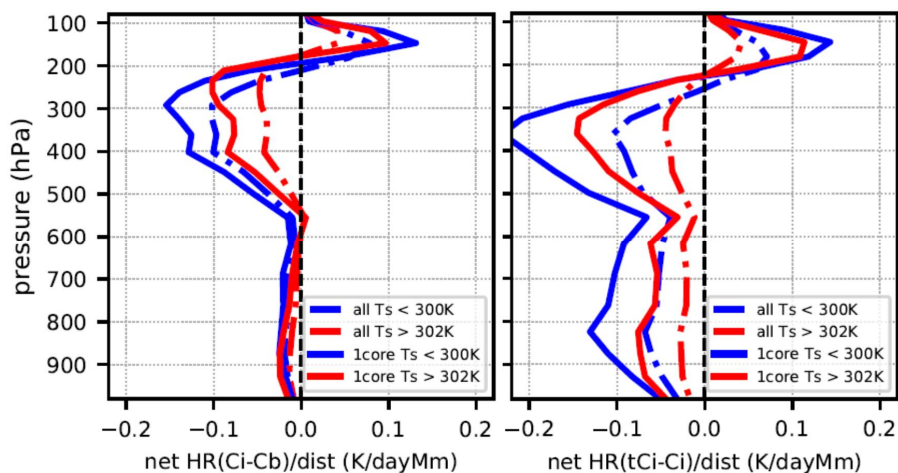
Figure 11: Difference of 24-hr mean net radiative heating between cirrus anvil and convective cores (left) and between surrounding thin cirrus and cirrus anvil (right), divided by the distance between the centers of these MCS parts, assuming circular systems, for MCSs with the 25% warmest areas of $T_{surf} < 300K$ and of $T_{surf} > 302K$, respectively. Compared are all MCSs, defined as UT cloud systems with at least one convective core, and those with only one convective core with a coverage within the MCS of at least 5%. Cloud observations at 1:30PM local time, with SW radiation normalized to 24 hours. Statistics of 15 years (2004-2018), averaged over 15N to 15S.
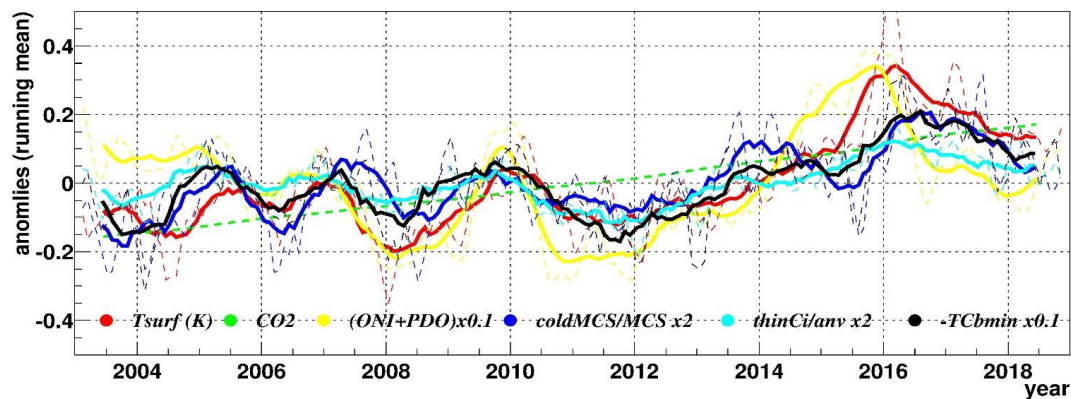
Figure 12: Time series of 12-month running means (bold lines) and 3-month running means of anomalies of global surface
920 **temperature (GISTEMP v4, Lenssen et al., 2019), ENSO index combined with Inter-decadal Pacific Oscillation index (each multiplied by 0.1), as well as coverage of cold MCSs over all MCSs (multiplied by 2), area of thin cirrus over area of total cirrus anvil (multiplied by 2) and minimum convective core temperature (in K multiplied by -0.1).**
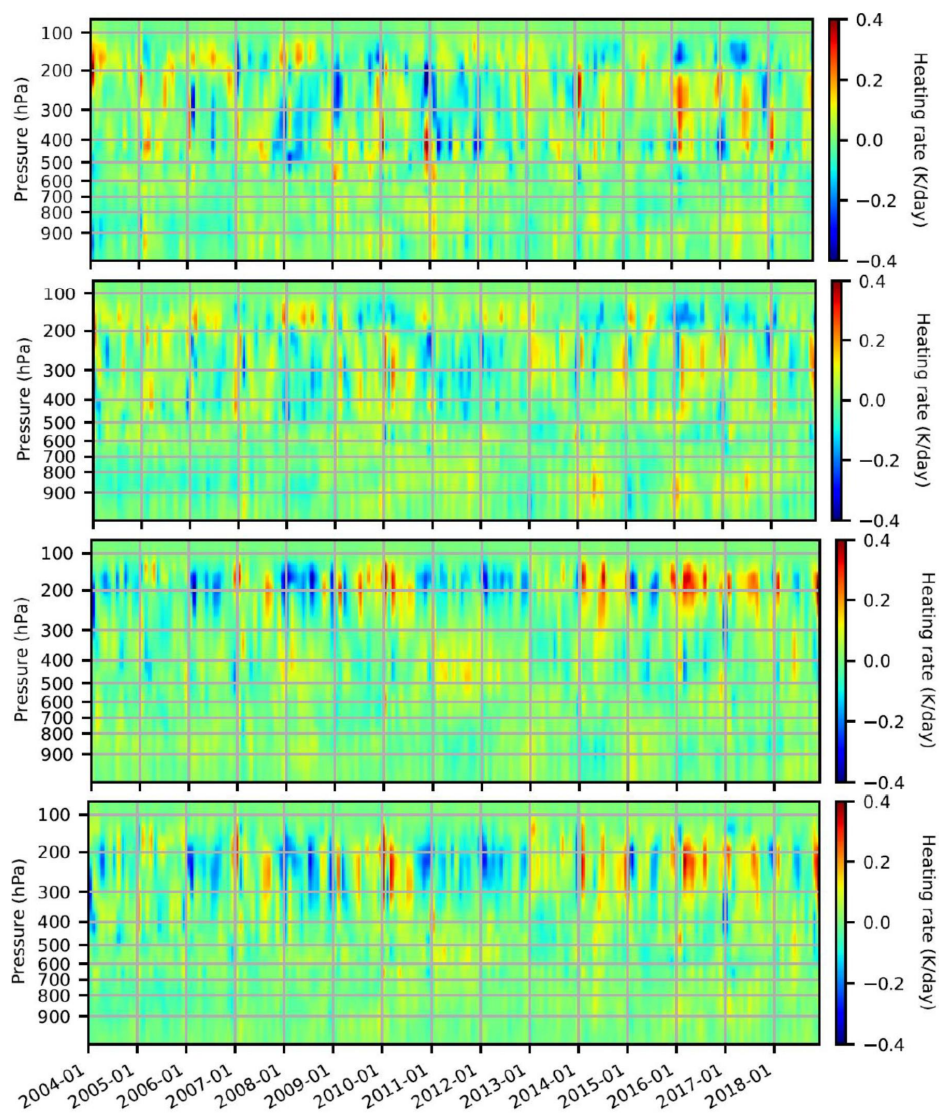
Figure 13: Time series of deseasonalized anomalies of heating / cooling effect of MCSs, when present; from top to bottom: net during nighttime (1:30 AM LT), LW, SW and net during daytime (1:30 PM LT).
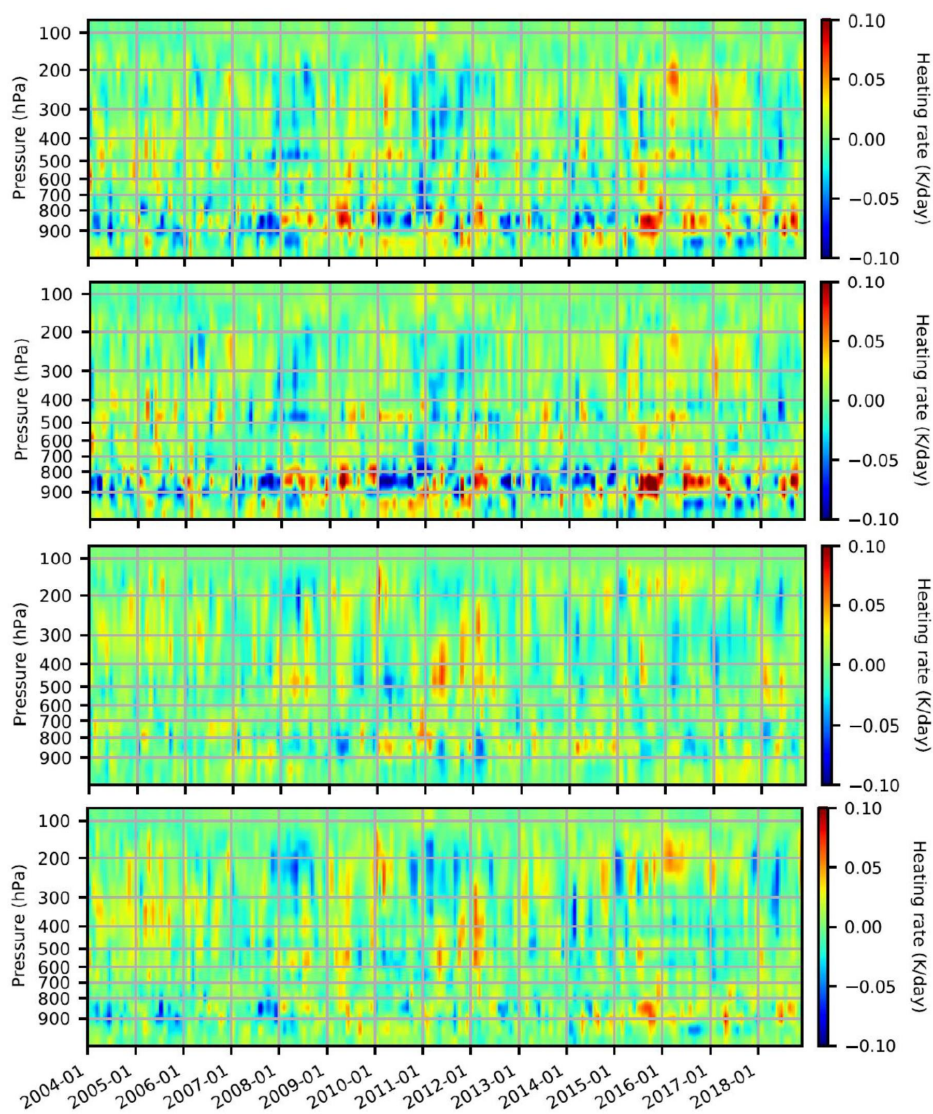
Figure 14: Time series of deseasonalized anomalies of cloud heating / cooling effect; from top to bottom: net during nighttime (1:30 AM LT), LW, SW and net during daytime (1:30 PM LT).

930